Journal of Sound and Vibration 645 (2026) 120097

Contents lists available at ScienceDirect

Journal of Sound and Vibration

journal homepage: www.elsevier.com/locate/jsvi

Predicting damage evolution via resonant frequencies in three-point bending tests: Experiments and LDEM simulations

G. Birck [a], G. Piana [b], W. Almeida [c], I. Iturrioz [a], G. Lacidogna [b,*]

[a] Department of Mechanical Engineering, Federal University of Rio Grande do Sul, Porto Alegre, Rio Grande do Sul, Brazil
[b] Department of Structural, Geotechnical and Building Engineering, Politecnico di Torino, Turin, Italy
[c] School of Engineering, Federal University of Rio Grande, Rio Grande, Rio Grande do Sul, Brazil

ARTICLE INFO

Keywords:
Lattice discrete element method (LDEM)
Failure prediction
Resonance frequencies
Vibration modes

ABSTRACT

In the present study, the crack propagation process in pre-notched concrete beams subjected to three-point bending was monitored by tracking variations in resonant frequencies. The tests were conducted under displacement-controlled conditions until final failure, using an incremental loading procedure. At each load step, the beam was subjected to impulse excitation, and the response was recorded by sensors positioned along the beam. A signal-processing methodology based on the Fast Fourier Transform (FFT) was then applied to extract the resonant frequencies from the recorded data. To complement the experimental analysis, a numerical investigation was performed. A version of the Lattice Discrete Element Method (LDEM) was implemented to simulate damage progression. The damage state obtained from the LDEM simulation was subsequently imported into a Finite Element Method (FEM) solver to perform modal analysis, providing additional dynamic characteristics such as mode shapes and resonant frequencies for direct comparison with the experimental results. The changes in resonant frequencies and mode shapes obtained from both the numerical and experimental analyses were compared. The results demonstrate that these dynamic characteristics are effective for monitoring damage evolution in the structure and predicting final failure. Emphasis is placed on the role of numerical simulation in supporting the interpretation of the experimental damage process.

1. Introduction

A variety of approaches exist for detecting and monitoring structural damage based on a system's dynamic response. Acoustic emission (AE) techniques, as described by [1], involve recording transient elastic waves using surface-mounted sensors. These signals are generated by sudden internal material responses, typically triggered by external excitation such as mechanical loading or thermal variations. Alternatively, ultrasonic waves can be actively propagated through a structure, and deviations in their propagation characteristics may indicate the presence of damage or other structural changes, as recently reviewed by [2].

When a structure can be considered a waveguide, i.e., when at least one of its dimensions is effectively infinite compared to the others, its wave propagation characteristics can be exploited to detect, monitor, and locate damage. Extensive literature exists on this subject, notably the work of [3].

It is well established that changes in structural stiffness are reflected in variations of modal parameters, particularly natural frequencies and mode shape curvatures. Within this framework, Dynamic Identification (DI) techniques are widely employed to extract

* Corresponding author.
E-mail address: giuseppe.lacidogna@polito.it (G. Lacidogna).

https://doi.org/10.1016/j.jsv.2026.120097
Received 5 March 2026; Received in revised form 19 August 2026; Accepted 28 August 2026
Available online 30 August 2026

such parameters from time-domain measurements of displacement, strain, velocity, or acceleration. A comprehensive treatment of this approach can be found in [4]. Numerous reviews in this area are available; among others, we highlight [5], which reviewed frequency-based damage detection methods and established natural frequency changes as important global indicators of structural integrity, [6], which demonstrated that flexibility matrix variations obtained from modal parameters can effectively localize structural damage, and the more recent work of [7], which developed an eigenvalue problem-based inverse approach for storey-level damage detection in high-rise buildings, combining modal data and Guyan condensation to identify structural stiffness changes using limited vibration measurements.

All the aforementioned methodologies have been significantly advanced over the past two decades through integration with data-driven techniques such as neural networks, deep learning, and other heuristic methods. A representative example of this integrated approach can be found in [8].

More recently, vibration-based structural health monitoring has evolved beyond the exclusive use of conventional modal indicators. The following examples illustrate some alternatives: the work conducted by [9] demonstrated the effectiveness of modal curvature variations for damage localization in reinforced concrete bridges subjected to progressive damage, while [10] proposed a framework based on modal flexibility and modal strain energy for damage detection in asymmetric building structures. Full-scale investigations conducted by Aras and co-workers [11,12] further showed that progressive structural damage and column-loss scenarios produce measurable changes in natural frequencies, mode shapes, and even the emergence of new vibration modes. These studies confirmed the potential of modal parameters as reliable indicators of structural deterioration and damage progression.

Building upon these foundations, recent research has increasingly incorporated advanced signal-processing and data-driven methodologies to improve damage sensitivity and robustness. In their study, Kang et al. [13] combined Variational Mode Decomposition and multi-source fusion of acceleration and strain measurements for structural damage identification, whereas [14] proposed a sparse damage identification framework based on multi-metric fusion and nuclear norm regularization. As noted in recent literature, the authors of [15] employed hierarchical knowledge transfer and Transformer-based architectures for reconstructing missing structural response data, while [16] developed a multi-scale deep-learning framework for extracting dynamic features from limited vibration measurements. Together, these contributions illustrate a clear transition from traditional modal parameter tracking toward intelligent vibration-based monitoring frameworks capable of integrating physical interpretation, feature extraction, data fusion, and machine learning techniques.

The use of numerical simulations to assess the performance of damage monitoring methodologies has been addressed in several studies, such as [17] and [18]. For structures made of quasi-brittle materials such as concrete, rock, or composites, numerical methods capable of simulating spontaneous fracture are of particular interest. Several options are available:

(i) In geomechanics, the foundational work of Cundall and Strack [19] is seminal. They proposed a method suitable for analyzing soils and other particulate systems, in which individual particles (e.g., sand grains) are modeled as discrete elements interacting through normal and tangential constitutive laws. A comprehensive review of the Cundall approach is provided by [20].
(ii) A different approach, widely used in biology and chemistry to examine atomic-level interactions, is Molecular Dynamics (MD). Conceptually similar to Cundall's approach, in MD each nodal mass represents an atom, and interatomic force functions must be prescribed. Reviews of the MD method have been published by [21] and [22]. Other variants of this approach employ nodes representing a supra-atomic organization, such as entire molecules, as adopted by [23] and, more recently, by [24].
(iii) Inspired by these ideas, Silling [25] introduced the Peridynamic theory as a nonlocal continuum formulation based on integral equations for modeling discontinuities and fracture. Subsequently, Silling and Askari [26] developed a meshfree numerical framework that enabled the simulation of damage localization and dynamic crack propagation through bond-breaking mechanisms. This method has been widely used in the last decade to simulate fracture and fragmentation, as described by [27] and [28]. Peridynamic theory has been recently employed to simulate acoustic emission in solids [29]. Several Discrete Element Methods similar to the Peridynamic approach have been proposed by other authors. State-of-the-art papers presenting different alternatives include [30–32].

Another version of the Discrete Element Method, which may be regarded as a particular case of Peridynamics, is the Lattice Discrete Element Method (LDEM), originally proposed by Riera in 1984 [33]. In this method, discrete masses are assigned a density associated with the discretization level. Force interactions between nodes are represented through a fixed arrangement of connecting bars, which results in a superposition of interaction forces. Explicit expressions can be derived to establish the equivalence between a mechanical solid structure and the corresponding spatial truss discretization. A nonlinear constitutive law for the bars is introduced to represent damage evolution and spontaneous fracture. The resulting spatial discretization yields a system of equations of motion, which must be integrated numerically using an explicit time-integration scheme.

This particular version of the Discrete Element Method has been employed by some of the present authors to simulate acoustic emission tests in studies such as [34,35], and, more recently, Tanzi et al. [36], as well as to simulate wave propagation in solids [37].

Previous studies by the authors have demonstrated the potential of combining Acoustic Emission (AE) and vibration-based monitoring techniques for damage assessment in concrete structures. In an initial investigation, AE activity and modal frequency variations were simultaneously monitored in pre-notched concrete beams subjected to four-point bending, revealing strong correlations between crack propagation, emitted energy, and stiffness degradation inferred from modal parameters [38]. Subsequently, the methodology was extended to three-point bending tests, where resonant frequency variations were combined with finite element simulations to estimate crack advancement and monitor damage evolution throughout the loading process [39]. Although these studies demonstrated the feasibility of correlating AE data and dynamic characteristics with damage progression, this second publication [39] clearly highlighted the potential predictive capability of resonant frequencies for tracking damage evolution and anticipating structural failure.

The novelty of the present study can be summarized in three aspects:

(i) The analysis of the experimental results previously presented in [38,39] is here thoroughly examined. Specifically, a pre-cracked concrete beam is loaded to failure, and a comprehensive experimental Dynamic Identification (DI) analysis is performed. The beam is tested under displacement-controlled loading up to collapse. The load is applied incrementally; at each step, the beam is excited by an impulse, and piezoelectric (PZT) sensors distributed along its length are used to identify resonant frequencies and the corresponding mode shapes. During the experimental campaign, numerous measurements of the resonance frequencies were taken at different load steps. All this information has now been used to present consolidated results regarding the change in resonant frequencies with damage evolution. Additionally, the measurements from several sensors allowed the identification of a spatial configuration of the modes and its relationship with the resonant frequency.

(ii) Damage progression is simulated using the Lattice Discrete Element Method (LDEM). The resulting damaged configurations obtained from the LDEM analysis are then used as input in a commercial Finite Element Method (FEM) package to compute changes in the natural frequencies of the selected modes.

(iii) Various aspects of the procedures detailed in (i) and (ii), applied to the pre-cracked concrete beam tested, could be applied to the analysis of structures of engineering interest.

The novelty of the present study lies in extending this framework by integrating experimental dynamic identification with numerical damage simulations based on the Lattice Discrete Element Method (LDEM). Particular emphasis is placed on establishing a direct relationship between the evolution of resonant frequencies, the progression of damage predicted by LDEM, and the approach to final failure.

To this end, a pre-cracked concrete beam is loaded to failure, and a comprehensive experimental Dynamic Identification (DI) analysis is performed. The beam is tested under displacement-controlled loading up to collapse. The load is applied incrementally; at each step, the beam is excited by an impulse, and piezoelectric (PZT) sensors distributed along its length are used to identify resonant frequencies and the corresponding mode shapes.

The damage progression is simulated using the Lattice Discrete Element Method (LDEM). The resulting damaged configurations obtained from the LDEM analysis are then used as input in a commercial Finite Element Method (FEM) package to compute changes in the natural frequencies of the selected modes.

The interpretation of the results is strengthened by combining numerical simulations with experimental measurements. A detailed description of the LDEM method is provided in the following section.

2. Implementation of the lattice discrete element method

In the current LDEM formulation, solid bodies are modeled as networks of one-dimensional elements with lumped masses concentrated at the nodes. These elements are designed to carry only axial forces. This concept was first introduced by [40], who proposed a three-dimensional regular truss structure obtained by repeating a cubic cell with nine nodes, capable of representing the mechanical behavior of an orthotropic elastic material. Fig. 1a illustrates this cubic cell and its nodal configuration.

This representation of an orthotropic elastic body was later adopted in [33] to address structural dynamic problems. In this formulation, the displacement of each node is defined along three orthogonal directions; in other words, each node has three degrees of freedom. An important parameter in this method is the length of the longitudinal and diagonal elements, represented by L_n and $L_d = \sqrt{3L_n/2}$, respectively. The relationship between an isotropic elastic material and the equivalent stiffness of the elements is given as follows:

$$EA_n = E\phi L_d^2 \tag{1}$$

$$EA_d = \frac{A_o 2\sqrt{3}}{3} \tag{2}$$

Here, E denotes Young's modulus, while $\delta = 9\nu/((4-8\nu))$ and $\phi = (9+8\delta)/(18+24\delta)$ are coefficients that relate the parameters defined for the longitudinal and diagonal elements to the properties of a linearly elastic solid. It is important to note that Poisson's ratio ν appears explicitly in the definition of the factor δ. When $\nu = 0.25$, the LDEM model becomes fully equivalent to an isotropic elastic solid.

The relationship between the stiffness of the LDEM elements and the properties of elastic solids was thoroughly investigated by [41]. The spatial discretization of the system leads to equations of motion that can be expressed in the standard form:

$$\mathbf{M}\ddot{\mathbf{u}} + \mathbf{C}\dot{\mathbf{u}} + \mathbf{F}_r(t) - \mathbf{P}(t) = 0 \tag{3}$$

In this equation, $\mathbf{u}$ represents the vector of generalized nodal displacements and their time derivatives. $\mathbf{M}$ is the mass matrix and $\mathbf{C}$ is the damping matrix; both are diagonal. The internal forces are represented by the vector $\mathbf{F}_r(t)$, while the external forces are represented by the vector $\mathbf{P}(t)$; both act on the nodal masses. Eq. (3) is uncoupled.

Internal material damping is assumed to vary linearly with the velocities of the nodal masses. The damping matrix $\mathbf{C}$ is given by $\mathbf{C} = 2\pi\zeta f_p \mathbf{M}$, where f_p is the frequency at the peak of the energy spectrum and ζ is the damping ratio. In this study, the damping coefficient is defined as $D_f = 2\pi\zeta f_p$.

To solve Eq. (3) in the time domain, a central finite difference scheme was employed for numerical integration. Since the nodal coordinates are updated at each time step, the formulation naturally accounts for large displacements when they occur.

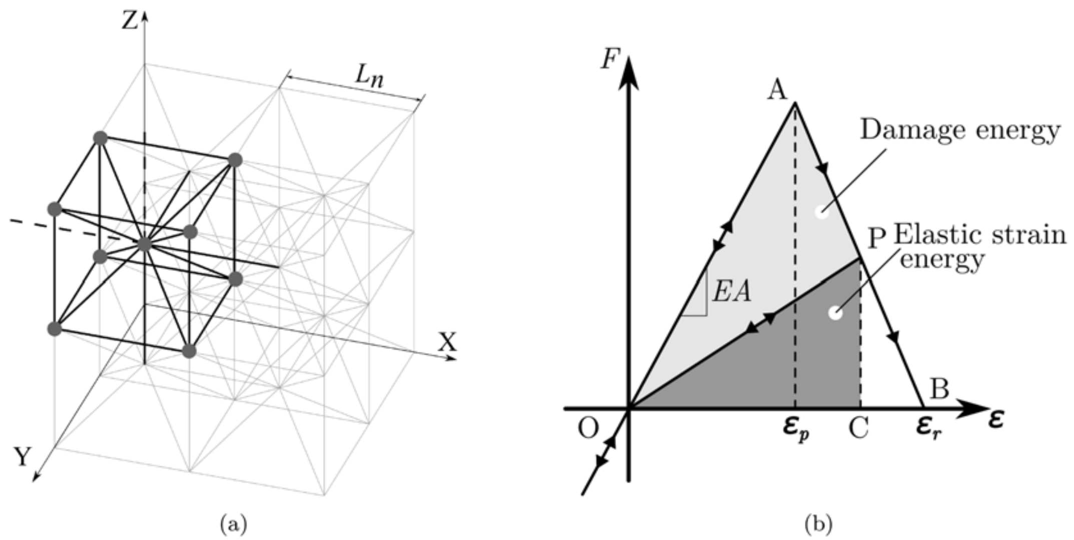

Fig. 1. Essential features of the LDEM model: (a) basic cubic cell within the LDEM lattice, (b) constitutive law adopted for the LDEM uniaxial elements.

The bilinear constitutive law proposed by [42], illustrated in Fig. 1b, has been widely applied in previous studies, demonstrating the ability of LDEM to capture the transition from diffuse damage to the formation of large cracks.

This constitutive model, applied to both longitudinal and diagonal LDEM elements, relates the axial force in each element to its uniaxial strain and accounts for the reduction in load-carrying capacity, thereby representing irreversible damage effects such as crack initiation and propagation.

According to this law, the energy required to fracture the element area of influence corresponds to the area under the force-strain curve (i.e., the area of triangle OAB in Fig. 1b). For a given point P on the force-strain curve, the area of triangle OAP represents the dissipated fracture energy, while the area of triangle OPC represents the recoverable elastic energy stored in the element. When the dissipated energy reaches the fracture energy associated with that element, it fails and loses its load-carrying capacity.

Under compressive loading in quasi-brittle materials such as concrete or rock, the material is assumed to behave in a linearly elastic manner, and failure occurs indirectly through tensile cracking. In general, this constitutive law can be modified without significant difficulty, if required.

Another important parameter is the strain corresponding to the maximum bar strength, which is computed as follows:

$$\varepsilon_p = \sqrt{\frac{G_f}{E d_{\mathrm{eq}}}} \tag{4}$$

where G_f represents the fracture toughness of the material. It is important to note the physical meaning of d_{eq}, which corresponds to the minimum crack length required for unstable crack propagation. In other words, if a crack with a length greater than d_{eq} develops in the structure, it will propagate unstably once a critical load level is reached [34]. To ensure the stability of the elementary constitutive bar, it is essential that $\varepsilon_r/\varepsilon_p > 1$.

The bar exhausts all its strength when ε is equal to or greater than ε_r (Fig. 1b), which is expressed as:

$$\varepsilon_r = \varepsilon_p d_{\mathrm{eq}} \left(\frac{A_i^*}{A_i}\right)\left(\frac{2}{L_i}\right) = \varepsilon_p k_r \tag{5}$$

Here, ε_p is the strain corresponding to the maximum strength of the bar, d_{eq} is the characteristic material length, and the index (i) denotes the type of bar – with ($i = d$) for diagonal bars and ($i = n$) for longitudinal bars. Moreover, L_i represents the bar length, A_i represents the bar cross-section, and A_i^* represents the equivalent fracture area of the bar under analysis. In the LDEM model, it was verified that, for longitudinal (normal) bars.

By equating the dissipated energy $U_{\mathrm{diss}}^{\mathrm{cubic}}$ in a cubic continuum cell of size L, associated with a fracture along a plane parallel to one of its faces, it is possible to determine the equivalent fracture area A_i^*. A detailed derivation can be found in [41].

In the LDEM model,it was verified that for the normal bars

$$k_r = \frac{\varepsilon_r}{\varepsilon_p} = \frac{0.26 d_{\mathrm{eq}}}{L} \tag{6}$$

then considering that k_r must be > 1, to keep the stability we must ensure that $d_{\mathrm{eq}} \geq 3.85 L_c$.

To obtain a more realistic representation of the material, G_f was modeled as a random field with a Weibull probability distribution given by:

$$\mathrm{prob}(G_f) = 1 - \exp[-(G_f/\beta)^\gamma] \tag{7}$$

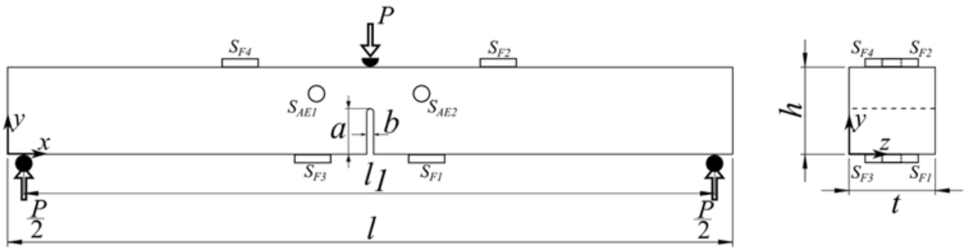

Fig. 2. Schematic representation of experimental setup.

Table 1
Main geometrical parameters.

l(mm)	l_1(mm)	h(mm)	t(mm)	a(mm)	b(mm)
840	780	100	100	50	4

where β and γ represent the scale and shape parameters, respectively. Details on how the spatial distribution of the random field is accounted for can be found in [43]. The LDEM approach described above has been widely applied to solve a variety of linear and nonlinear engineering problems. Typical applications include the analysis of shells and plates under impulsive loading [44,45], modeling the generation and propagation of earthquakes [35,46], and, as mentioned in the introduction, the simulation of acoustic emission problems [34–36].

3. Test description

3.1. Experimental test

Two concrete beams with identical dimensions were tested under three-point bending (TPB). Both beams were pre-notched at mid-span to half of their depth. A schematic of the setup and the geometric properties are shown in Fig. 2 and Table 1, respectively. The TPB tests were conducted following the specifications of the RILEM Technical Committee TC 50-FMC [47].

The compressive strength $f_c = 26.4$ MPa and mass density $\rho = 2310\,\mathrm{kg/m^3}$ were obtained by averaging measurements performed on five concrete cubic specimens with a side length of 160 mm. Young's modulus was $E = 30.57$ GPa. The mechanical properties were evaluated according to the Italian technical regulation [48]. Finally, the fracture energy of the same concrete was $G_f = 134.3$ N/m.

A servo-hydraulic MTS testing machine was used to test the specimens up to final failure under displacement control by imposing the vertical displacement of the hydraulic jack, while recording the load-displacement curve. Two testing procedures were followed:

(i) The displacement was continuously increased at a constant rate of 1 μm/s (hereafter referred to as Test 1).
(ii) The displacement was increased incrementally in several steps. At the end of each step, the specimen was excited by an impulsive force, and the free response was recorded by sensors to extract the resonant frequencies (hereafter referred to as Test 2).

The resonant frequencies in Test 2 were extracted using four JPR Plustone 400–403 piezoelectric pickups (outer diameter 20 mm, frequency range ~0–20 kHz, resonant frequency 6 ± 0.5 kHz, operating temperature range - 20 to + 50 °C, and weight ~1 g). The acquisition device was an AudioBox 1818VSL (PreSonus, Baton Rouge, LA, USA) with 8 channels, and the sampling frequency was set to 48 kHz. The locations of the pickups, denoted SF1 to SF4, are indicated in Fig. 2.

Acoustic emission data were collected during the test. Two sensors, denoted S_{AE1} and S_{AE2}, with locations indicated in Fig. 2, were used for data acquisition. A detailed description of these tests, including the equipment used and the acoustic emission analysis, is available in the previous publications [38,39]. The present paper examines the relationship between resonant frequency evolution and damage progression in detail, with emphasis on the results of Test 2.

In Fig. 3a and b, the initial and final configurations of Test 2 are presented. Additionally, in Fig. 3c and d, details of the final configuration and the configuration immediately before collapse are shown. In Fig. 3d, the main fissure emanating from the notch is highlighted with a yellow ellipse, while the red ellipses indicate the regions of typical damage produced in the compression area.

The load-mid-span deflection curves for both tests are shown in Fig. 4, which also includes a polynomial interpolation of the Test 2 data (dashed line). The load drops and subsequent recoveries in Test 2 resulted from pauses required to perform resonant frequency measurements (i.e., interruptions in the imposed displacement followed by a loading restart). The test included ten such pauses, creating eleven loading steps, with the final step leading to specimen failure. These load fluctuations are therefore a direct artifact of the experimental procedure.

3.2. Finite element model of TPB resonant frequencies

Resonant frequencies were measured experimentally following the previously described procedure, which, for Test 2, required pauses in the loading protocol. To interpret the experimental data, a three-dimensional finite element (FE) model of the beam was

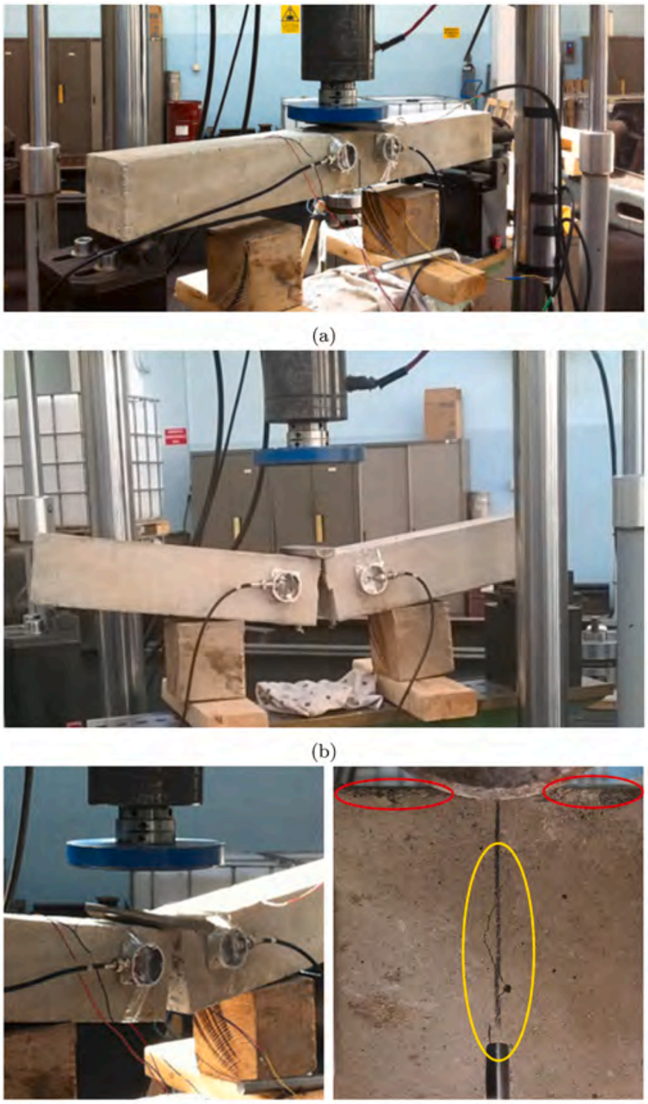

(a)

(b)

(c) (d)

Fig. 3. TPB test carried out as Test 2: (a) initial configuration, (b) final configuration, (c) isometric view of the beam in the final configuration, (d) detail of the cracking immediately before failure. The yellow ellipse shows the main fissure emanating from the notch, while the red ellipses indicate ruptures in the compression zone. (For interpretation of the references to color in this figure legend, the reader is referred to the web version of this article.)

developed using the commercial software ANSYS [49]. The model employed 20-node brick elements (SOLID186) and assumed linear elastic material behavior with the following properties: Young's modulus $E = 30.57$ GPa, Poisson's ratio $\nu = 0.25$, and density $\rho = 2310\,\mathrm{kg/m^3}$. An element size of 4 mm was adopted, and the geometry was consistent with the dimensions reported in Table 1. The model boundary conditions are shown in Fig. 5, and its first ten vibration modes are listed in Table 2. Four of the five modes, highlighted in Fig. 6, are particularly relevant for the subsequent analysis of the experimental results. The first mode is lateral; for this reason, it is not activated in the present analysis.

3.3. Experimental analysis of resonant frequencies during beam damage progression in Test 2

The analysis focused on monitoring four specific vibration modes: the first two vertical bending modes (Modes 2 and 3), the torsional mode (Mode 6), and a higher-order vertical bending mode (Mode 10).

Fig. 7 presents results from a previous study [39], showing the evolution of the resonant frequencies for Modes 2 (antisymmetric), 3 (symmetric), and 10 (antisymmetric), as illustrated in Fig. 6. According to the data reported in [39], the resonant frequencies decreased significantly during the test: by 8.9% for Mode 2, 26.6% for Mode 3, and 13.2% for Mode 10.

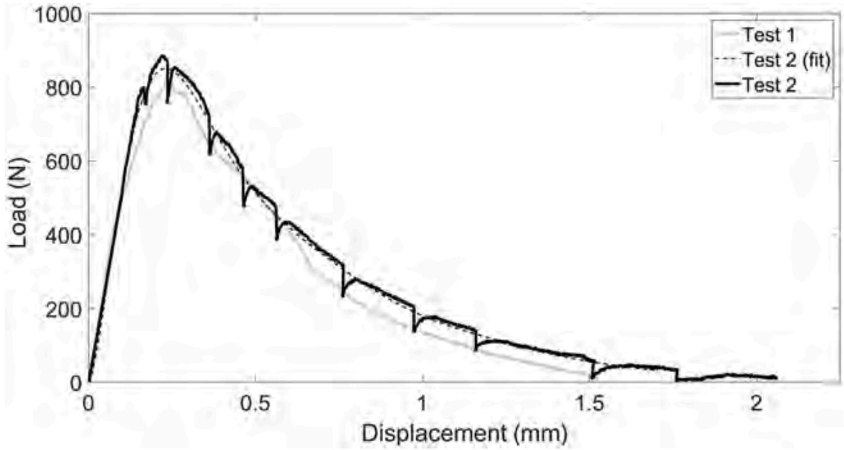

Fig. 4. Experimental load vs. displacement curves.

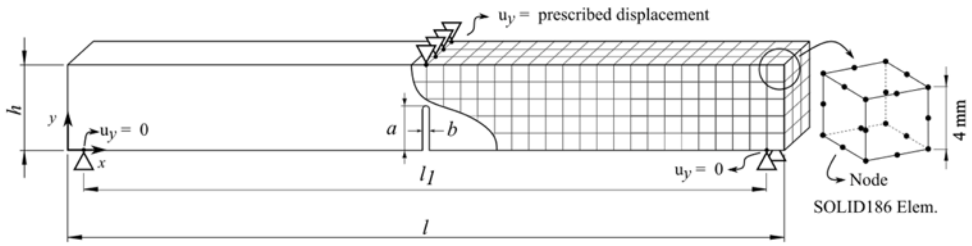

Fig. 5. FEM model using the solid elements.

Table 2
First ten modes of vibration, for a/h = 0.5, frequencies in Hertz.

Mode	Frequency	Mode	Frequency
1	457.7	6	**1870.6**
2	**958.8**	7	1943.2
3	**1050.5**	8	2209.6
4	1265.4	9	2753.7
5	1464.7	10	**2988.6**

Furthermore, Fig. 7 reveals a frequency crossover phenomenon after a certain level of damage was reached. Initially, Mode 2 exhibited an antisymmetric shape, while Mode 3 was symmetric. However, as damage progressed, the mode shapes switched, with Mode 2 becoming symmetric and Mode 3 becoming antisymmetric.

At a beam displacement of 0.17 mm, the experimentally identified frequencies were 1018.9 Hz for Mode 2, 1145.8 Hz for Mode 3, and 3279.45 Hz for Mode 10. It is important to note that the frequencies predicted by the finite element model (Table 2) are 5-10% lower than the experimental measurements. This discrepancy is likely attributable to the impulse energy from the hammer impact being insufficient to overcome friction at the supports. Given that the beam is made of concrete, such support friction is expected to influence the dynamic response, particularly under low-energy excitations.

The experimental data were reanalyzed to identify the vibration modes and their corresponding frequencies for comparison with the numerical results. The reanalysis procedure, illustrated in Fig. 8, consisted of the following steps:

(i) **Step Loading:** The load was applied in discrete increments. After reaching each target load level, the loading process was temporarily paused.

(ii) **Impact Excitation and Signal Acquisition:** Five impact excitations were applied to the beam using a rubber hammer. The excitations were always applied in the vertical direction, with three at the top and two at the bottom. The excitations were applied between the supports and the SF_n sensors, on both sides (left and right). Care was taken to never apply the excitation on the central bar in order to activate the torsional mode. For each impact, the response signals were recorded by all four resonant sensors (SF1-SF4), as indicated in Fig. 2. Consequently, a total of 20 signals (5 impacts × 4 sensors) were obtained for evaluation at each load step. A representative time-domain signal is presented in the first panel of Fig. 8.

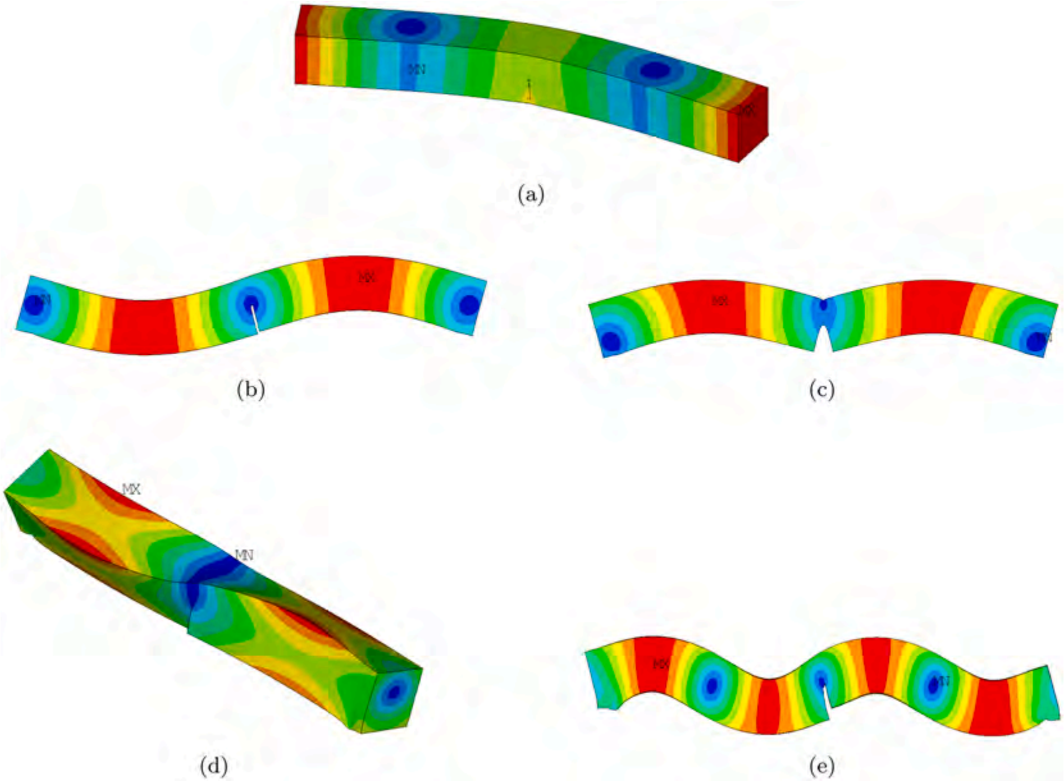

Fig. 6. Behavior of the vibration modes obtained numerically: (a) Mode 1 (457.682 Hz) exhibits lateral movement. (b) Mode 2 (958.8 Hz) and (c) Mode 3 (1050.5 Hz) correspond to the first two vertical bending modes. (d) Mode 6 (1870.6 Hz) and (e) Mode 10 (2988.6 Hz) correspond to a torsional mode and a vertical bending mode, respectively.

(iii) **Spectral Analysis:** The Power Spectral Density (PSD) was computed for each of the 20 signals in order to identify the frequency content, as illustrated in the second panel of Fig. 8.
(iv) **Peak Identification:** The frequency range of each PSD was divided into three bands: 300-799 Hz (marked with an asterisk *), 800-1600 Hz (marked with a circle $\circ$), and 2200-3600 Hz (marked with a triangle $\triangle$). Within each band, the three highest peaks were identified. The data points were then color-coded according to the sensor that recorded each signal, as schematically illustrated in the third panel of Fig. 8.
(v) **Frequency Tracking:** As shown in the final two panels of Fig. 8, this process generated 60 candidate frequency points per load step (5 impacts $\times$ 3 frequency candidates per band $\times$ 4 sensors). The persistence of a given frequency across multiple load steps reveals a clear trend line, demonstrating how the resonant frequencies decrease as damage progresses in Test 2.

The outcome of the procedure illustrated in Fig. 8 is summarized in Fig. 9, which presents the resonant frequency as a function of mid-span displacement, with loading pauses explicitly indicated. The plot uses colors to distinguish the sensors and marker shapes (asterisk *, circle $\circ$, triangle $\triangle$) to represent the different frequency ranges. Key findings from Fig. 9 include:

(i) The identification of the four target modes shown in Fig. 6.
(ii) A clear mode transition between the fifth and sixth load steps for the first two vertical modes.
(iii) Successful capture of the frequency variation of the torsional mode.

The trend lines are assigned as follows: Modes 2 and 3 (blue and black), Mode 6, torsional (cyan), and Mode 10, vertical antisymmetric (red). The green line represents a mode that was not analyzed in this study.

Fig. 9 illustrates the frequency variation as a function of the mid-span displacement across 10 sequential stages (Stops 01 to 10), which represent the damage propagation in the structure.

The analysis is divided into three distinct frequency intervals, with each marker type indicating one of these bands:

- **Asterisk** ($*$): 300 to 799 Hz range.
- **Circle** (**O**): 800 to 1600 Hz range.
- **Triangle** ($\triangle$): 2200 to 3600 Hz range.

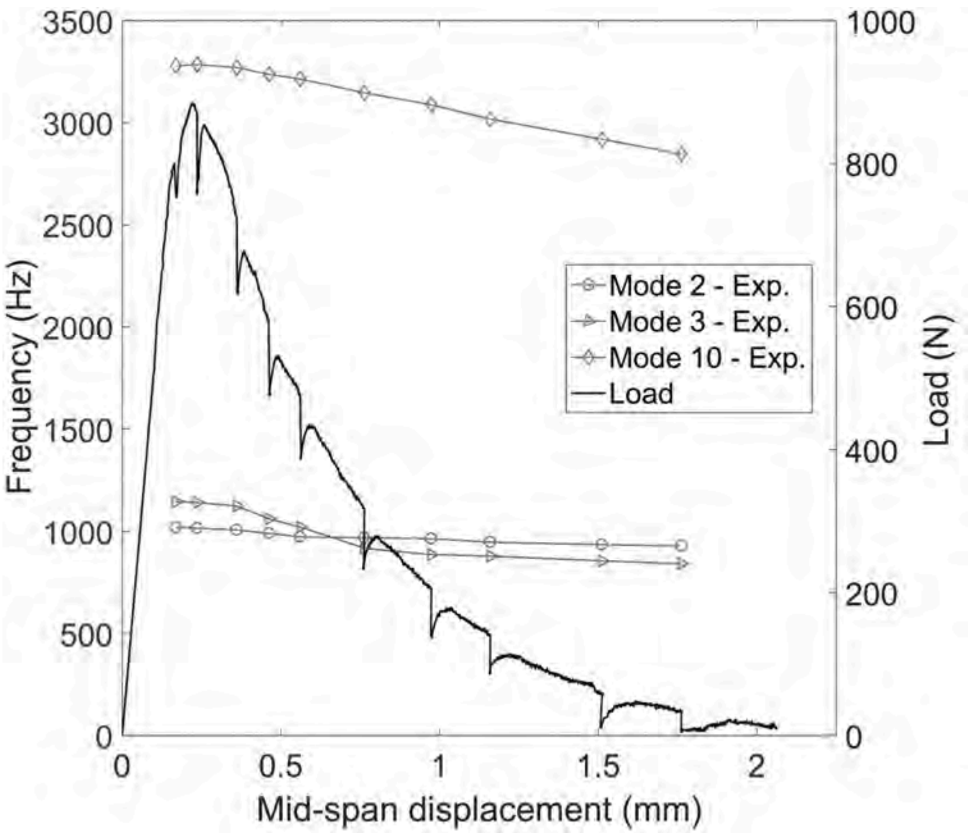

Fig. 7. Variation of resonant frequencies identified in Test 2. Adapted from [39].

Within each frequency band, FFT was performed to identify the peaks with the highest energy, specifically the 3 largest Power Spectral Density (PSD) peaks. The colors of the markers serve to identify the sensor from which the data were collected: **SF1 (red)**, **SF2 (green)**, **SF3 (blue)**, and **SF4 (violet)**.

Therefore, for each sensor (color) within a specific frequency interval (marker type), the graph plots exactly **3 identical markers**. These represent the 3 most dominant frequencies captured by that specific sensor in that particular analysis window.

3.4. Identification of vibration modes

To identify the vibration mode from a single impact using the rubber hammer, the Power Spectral Density (PSD) and the phase of the Fourier transform were computed for the signals acquired from the four sensors (SF1-SF4). By examining the phase at the resonant frequencies corresponding to the target modes shown in Fig. 6, it was possible to confirm whether an identified frequency truly represented one of these modes.

This verification process is illustrated in Fig. 10, which presents the analysis of the response to a single impact across all four sensors (SF1-SF4) at Stop 2. When the phases of the Fourier transforms for the displacement measurements at the spatial points (SF1-SF4) have the same sign, it indicates that these points are moving in the same direction. Conversely, opposite signs indicate that the sensors are moving in opposite directions. This information is useful for identifying the vibration mode associated with each measured frequency.

For each time-domain signal, the PSD and the phase of the Fourier transform were computed and are displayed in the center and right columns of Fig. 10, respectively. The resonant frequencies captured by each sensor (SF1-SF4), labeled P1 to P4, were identified from the PSD. It should be noted that resonant frequencies are not always identified by all sensors. Specifically, the second resonant frequency (P2) was not identified for SF1 in the analyzed signal, and the fourth resonant frequency (P4) was not detected in the signal from SF4.

Table 3 summarizes the phase signals obtained from the sensors during a single impact using the rubber hammer at the second stop. By comparing the direction of motion indicated in Table 3 with the studied modes presented in Fig. 11, it was verified that the experimental results were consistent in all cases.

For example, Fig. 11a shows Mode 2, in which sensors SF1 and SF2 move in one direction, whereas SF3 and SF4 move in the opposite direction. This observation is consistent with the first row of Table 3, which documents the sign of the sensor motions. The same procedure can be applied to the other modes shown in Fig. 11, confirming that all predicted modes are consistent with the experimental results.

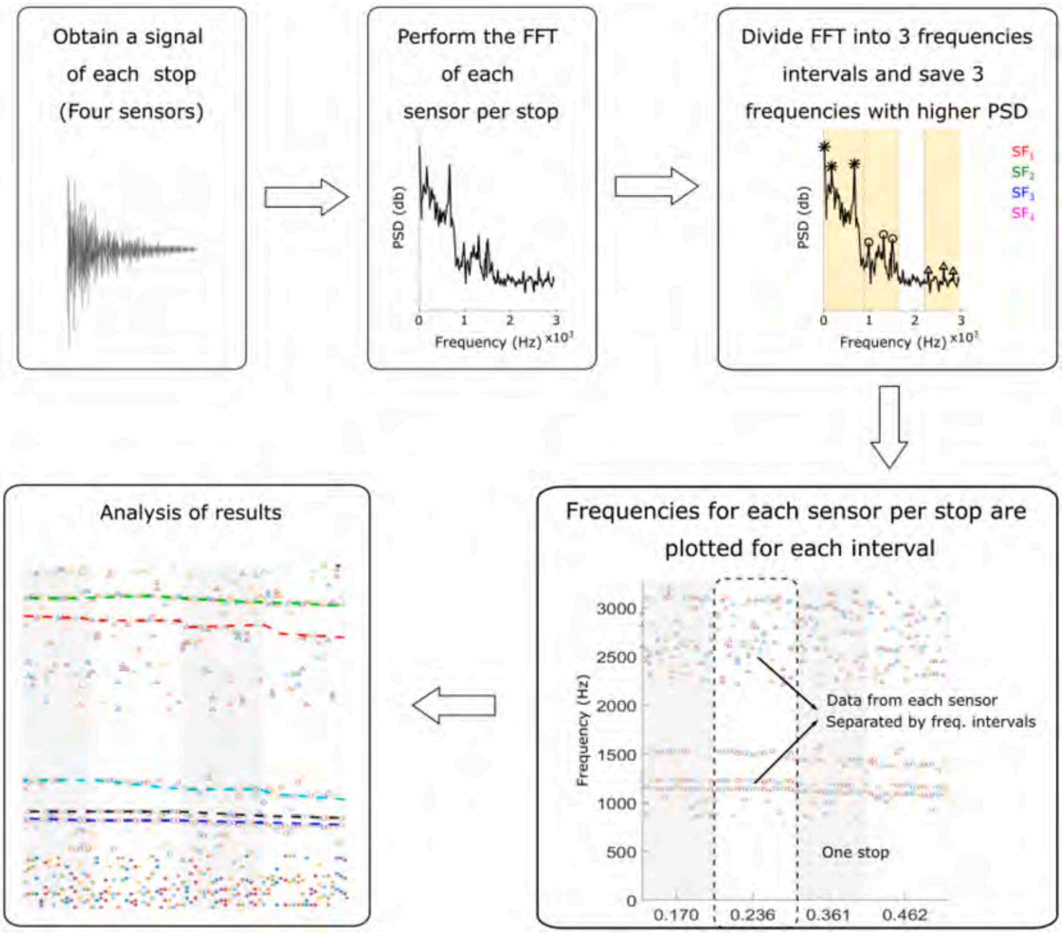

Fig. 8. Sequential reanalysis steps performed on the experimental data from Test 2 using frequency sensors SF1 (red), SF2 (green), SF3 (blue) and SF4 (violet). The colors correspond to the points indicated in Fig. 9. In the two bottom panels of the figure, the horizontal axis represents the mid-span displacement (mm). (For interpretation of the references to color in this figure legend, the reader is referred to the web version of this article.)

Table 3
Summary of the phase signal computed in Fig. 10. The asterisk (*) indicates that the resonant frequency was not found in this measurement.

	SF1	SF2	SF3	SF4
P1	(-)	(-)	(+)	(+)
P2	(*)	(+)	(+)	(+)
P3	(+)	(+)	(+)	(-)
P4	(-)	(-)	(+)	(*)

Using the described procedure, the four modes that were the focus of the present study were successfully identified.

4. Numerical analysis by LDEM

4.1. Model details

The beam was simulated using the Lattice Discrete Element Method (LDEM) with a three-dimensional model comprising 210 × 25 × 25 cubic modules, each with a side length of 4 mm. A notch was introduced by removing the lattice bars within the corresponding central cubic elements.

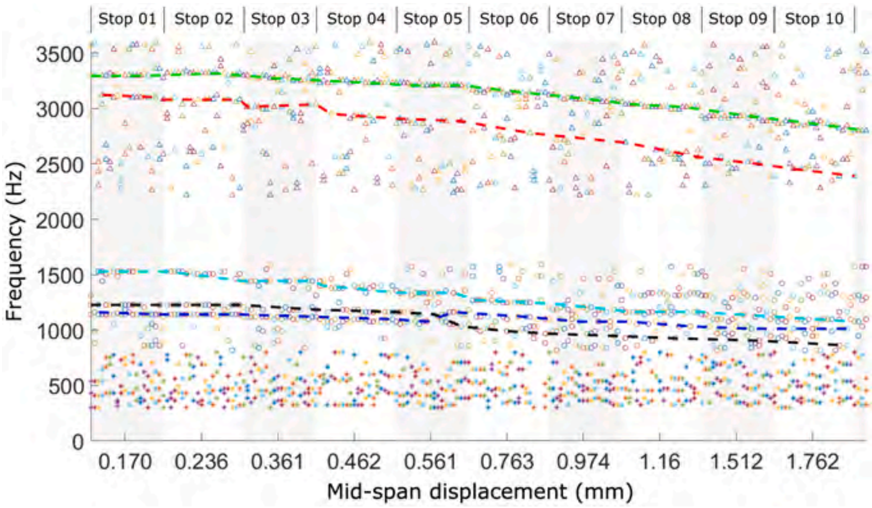

Fig. 9. Frequency tracking as a function of mid-span displacement across different damage propagation stages (Stops 01-10). Asterisk, circle, and triangle markers represent the three dominant frequencies (highest PSD peaks) extracted within the 300-799 Hz, 800-1600 Hz, and 2200-3600 Hz FFT bands, respectively. Marker colors identify sensors SF1 (red), SF2 (green), SF3 (blue), and SF4 (violet). Dashed lines highlight the identified modal trends. (For interpretation of the references to color in this figure legend, the reader is referred to the web version of this article.)

Table 4
Main LDEM parameters.

E (MPa)	ν	ρ (kg/m^3)	G_f (N/m)	CV (G_f)	L_n (mm)	d_{eq} (mm)
30.57	0.25	2310	134.3	65%	4	60

Fig. 12 presents the front view of the model, illustrating the boundary conditions and the loading location. Detail B in the same figure provides a close-up view of the notch configuration.

The loading was applied as a prescribed displacement, increased in linear steps at a low rate. The recorded displacement corresponds to the value at the upper support where the displacement was prescribed, as shown in Detail C of Fig. 12. The applied load was calculated by summing the reaction forces at the lower supports. The primary parameters used in the LDEM simulation are provided in Table 4.

Using the input parameters from the LDEM model and Eq. (3), the critical strain, ε_p, was calculated as 2.7×10^{-4}. The corresponding critical tensile stress, σ_t, was then obtained as $\varepsilon_p \times E = 8.3$ MPa. Furthermore, Eq. (5) was used to compute the ratio between the ultimate and critical strains, $k_r = \varepsilon_r/\varepsilon_p = 3.9$. These values fall within the admissible range for concrete.

4.2. Simulation of static response

Fig. 13 presents the load-displacement curves obtained from both the experimental test (Test 2) and the numerical simulation. The simulated curve closely reproduces the behavior observed in the experimental results. Furthermore, the final fracture pattern obtained from the simulation shows good agreement with the experimental observation, as demonstrated by comparing Fig. 14 with Fig. 3b–d at the peak load. Fig. 14 illustrates the broken and damaged bars at peak load, where the color scale indicates the time progression from the beginning to the end of the numerical test.

The energy balance for the simulated static response is presented in Fig. 15. The absence of abrupt changes in the curves indicates ductile or transitional system behavior. This result is expected, since a critical crack length of $d_{eq} = 60$ mm cannot be attained in this case. The transverse crack area is of the same order of magnitude as the characteristic cross-sectional dimension of the beam (100 × 100 mm). It is important to recall that a pre-existing crack is present, which makes it physically impossible for a main crack of this size to develop. Note that the kinetic energy in Fig. 15 is plotted on a different scale to make its variation during the simulation perceptible.

4.3. Simulation of natural frequencies

During the experimental testing, the procedure for obtaining the resonance frequencies required periodic stops. This is not necessary in the LDEM simulation. Instead, the complete state of the model, termed a “photograph”, is saved at regular time intervals. Each of these saved states is then processed using a Finite Element Method (FEM) solver to perform an eigenvalue analysis, from which the eigenfrequencies and corresponding mode shapes are obtained.

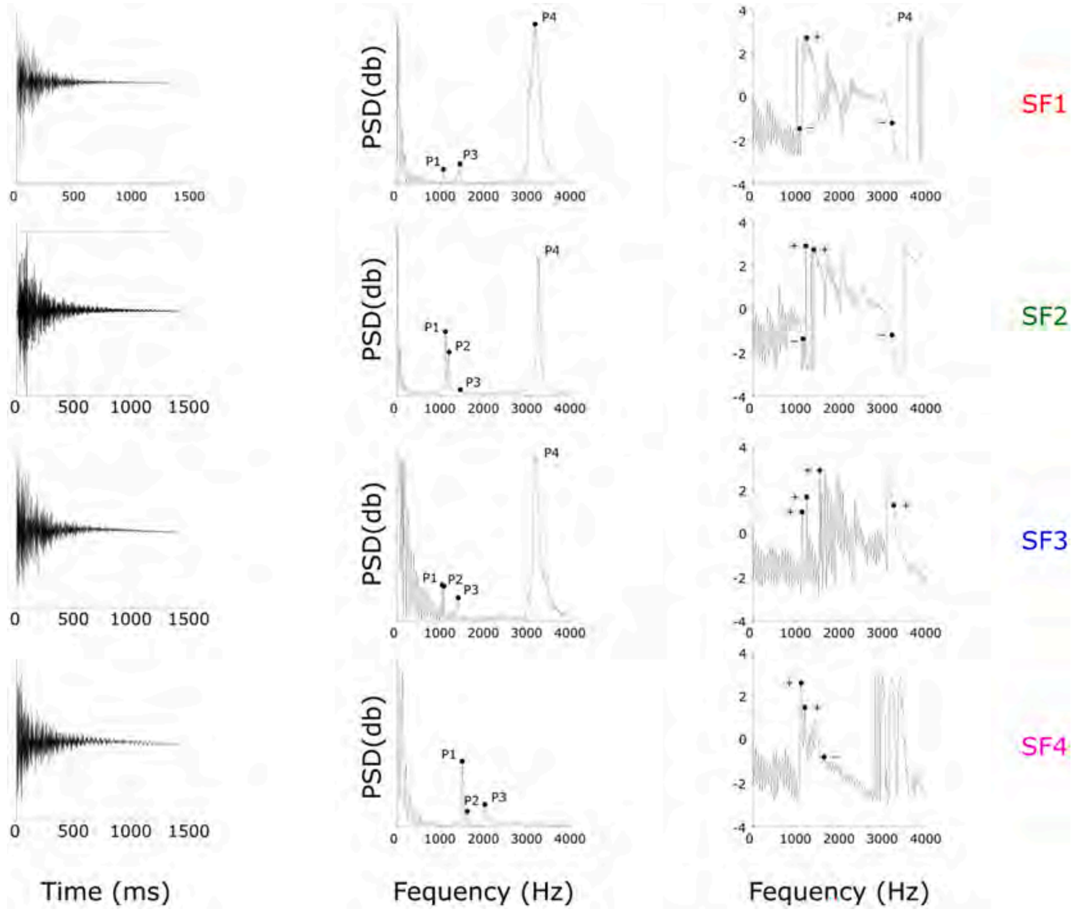

Fig. 10. Phase identification for each measurement point resulting from a single hammer impact at the second stop. The left column shows the time-domain signals from sensors SF1 to SF4. The central column displays the power spectrum, with the four frequencies used in the beam analysis (P1 to P4) indicated. The right column presents the phase in the frequency domain, indicating the direction of motion for each resonant frequency. In all figures, the horizontal axis labels for the left, central, and right columns appear only once, at the bottom. The vertical axes for the left and right columns are in arbitrary units.

The FEM model was implemented in the commercial software ANSYS [49] using LINK180 elements, which are uniaxial tension-compression elements with three translational degrees of freedom per node. MASS21 elements were also employed to represent concentrated nodal masses. The material properties (Young's modulus, E, and Poisson's ratio, ν) were assumed to be uniform for all bar elements. To account for damage progression obtained from the LDEM simulation, the cross-sectional area of each bar in the FEM model was individually adjusted for each "photograph". This approach ensures that the axial stiffness of each element correctly reflects its current level of damage, since a damaged bar can no longer sustain the same load as an intact one.

The overall scheme for obtaining the resonance frequencies from the LDEM "photographs" using this FEM-based approach is illustrated in Fig. 16.

4.4. Model validation

To validate the modal analysis method based on LDEM data, a comparative analysis was conducted between the LDEM approach (with the modal analysis performed via FEM) and a conventional FEM model. The comparison involved the notched beam, with dimensions identical to those reported in Table 1.

A reference model was developed using the ANSYS FEM package with SOLID186 three-dimensional brick elements. The mesh size was set to 4 mm to correspond directly to the elementary cubic module used in the LDEM model.

The resulting resonance frequencies obtained from both models, the brick-element FEM model and the truss-based LDEM model, are presented in Table 5. The maximum difference observed between the two sets of results was 0.55%, occurring for the second vibration mode. Furthermore, the corresponding mode shapes were identical for all analyzed modes.

From this point onward, the frequencies and mode shapes obtained from the LDEM model are considered valid, since the differences between the FEM and LDEM results are within admissible limits.

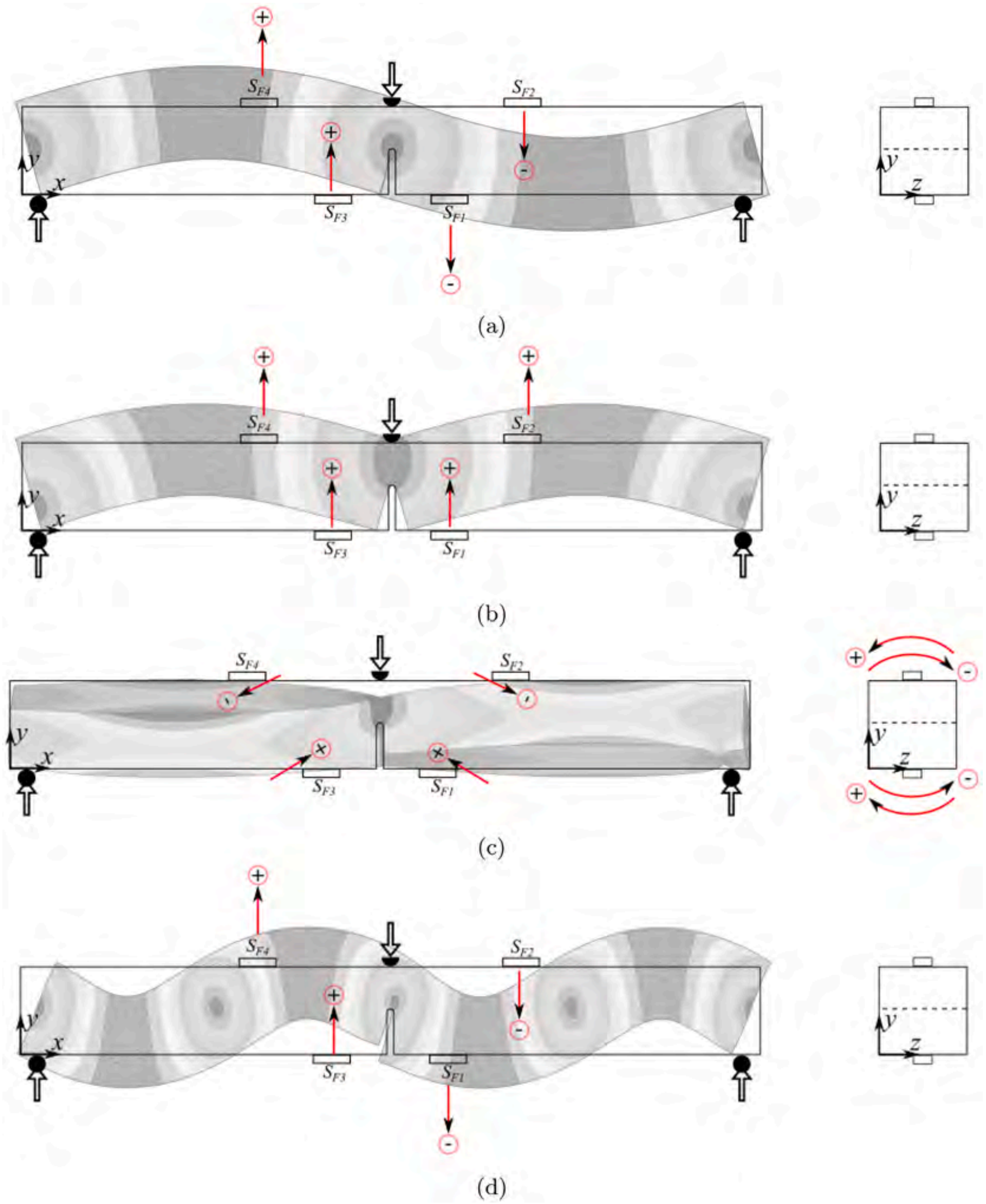

Fig. 11. Sensor phase across different vibration modes: (a) antisymmetric vibration mode (P1), (b) symmetric vibration mode (P2), (c) torsional vibration mode (P3), and (d) antisymmetric vibration mode at higher frequencies (P4).

5. Comparison between experimental and numerical results

The load-displacement curves in Fig. 13 demonstrate similar behavior for the experimental test and the LDEM simulation. The final damage patterns are also comparable, with failure in both cases resulting from the initiation and propagation of cracks at the mid-span notch, as shown in Fig. 3 for the experimental test and in Fig. 14 for the LDEM simulation.

Fig. 17 compares the vertical resonant frequencies obtained experimentally with those calculated numerically using the procedure described in Section 4.3. The resonant frequencies predicted by the LDEM simulation are consistently lower than the experimental values. Despite this discrepancy, both datasets exhibit similar trends, including a progressive decrease in frequency with damage evolution and an inversion of the first two vertical mode shapes. However, this mode inversion occurs at an earlier stage in the numerical model.

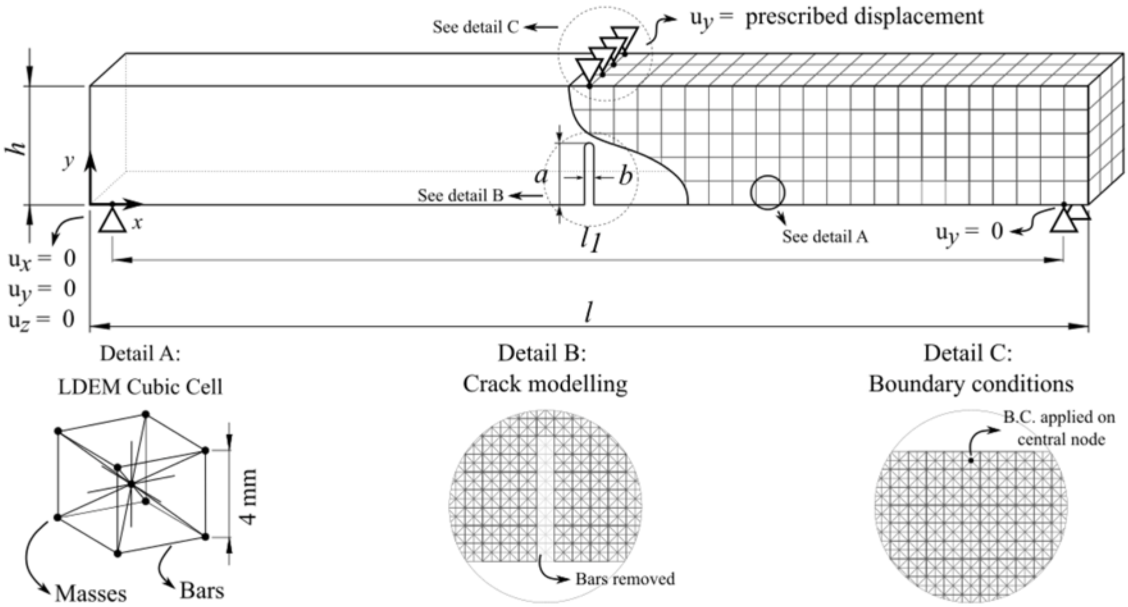

Fig. 12. Schematic LDEM beam Model.

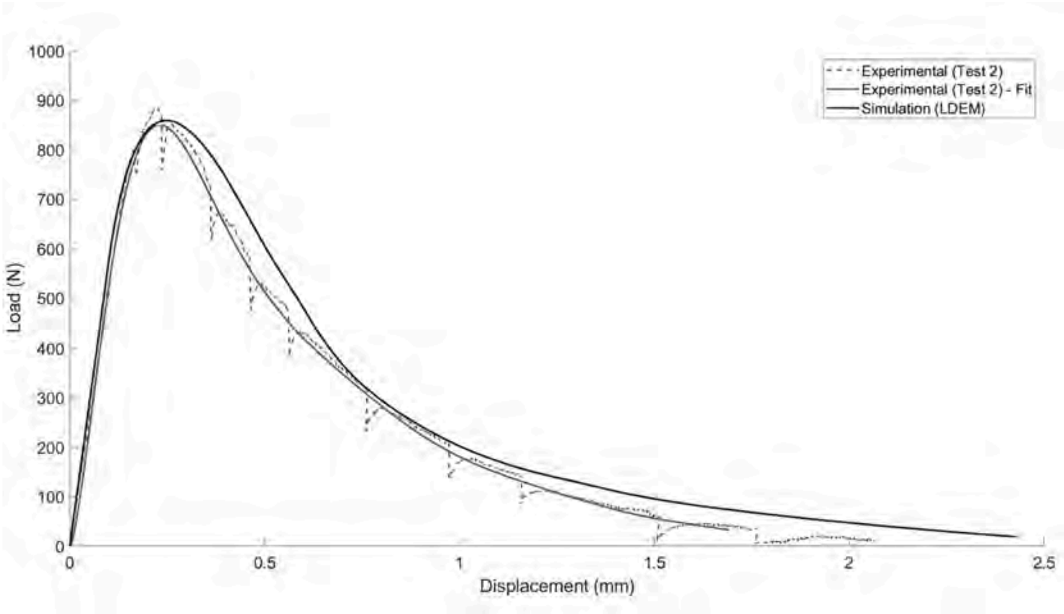

Fig. 13. Load-displacement curves for Test 2, Test 2 (fit), and the numerical simulation.

These differences suggest that the numerical model may be overly simplified and therefore unable to fully capture the damage evolution observed in the real beam during Test 2. One of the main contributing factors is likely the influence of nonlinear behavior associated with progressive damage on the resonant frequencies. A more detailed investigation of these aspects will be addressed in future work.

The evolution of the numerically obtained resonant frequencies is examined in detail below. Since the mode shapes associated with the first two vertical frequencies evolve throughout the loading process in both the experimental and numerical results, these modes are the focus of Fig. 18.

In this figure, the frequencies are normalized by their initial values ($F1/F1_0$ and $F2/F2_0$, where $F1_0$ and $F2_0$ correspond to the undamaged beam at zero mid-span displacement). The ratio between the two frequencies ($F2/F1$) is also plotted. As shown in Fig. 18, the two mode shapes change near the maximum load, accompanied by a change in the slope of the F2/F1 curve. This behavior may provide a practical criterion for identifying the structural limit of the beam or for estimating its remaining service life. However, it

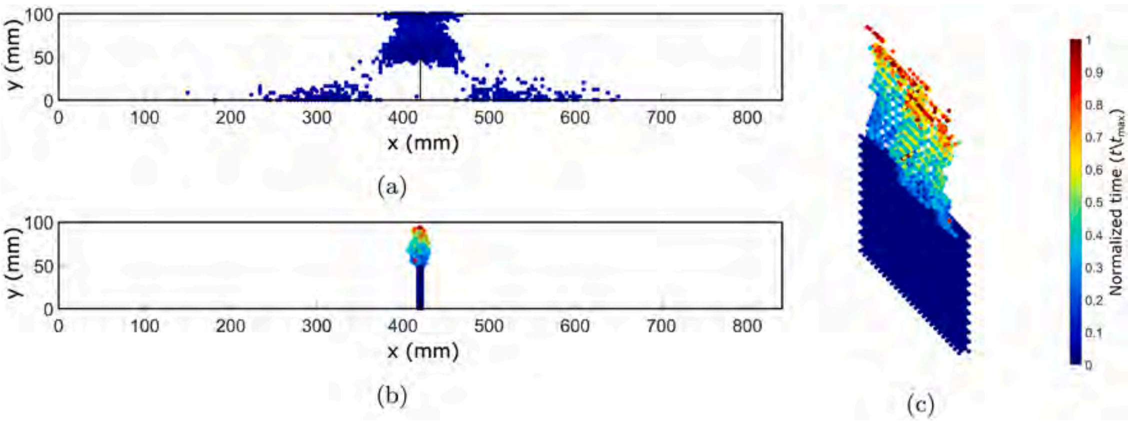

Fig. 14. Representation of damaged and broken bars over time: (a) damaged bars from the beginning up to peak load, (b) broken bars from the start to the end of loading, and (c) three-dimensional view of broken bars from the start to the end of loading.

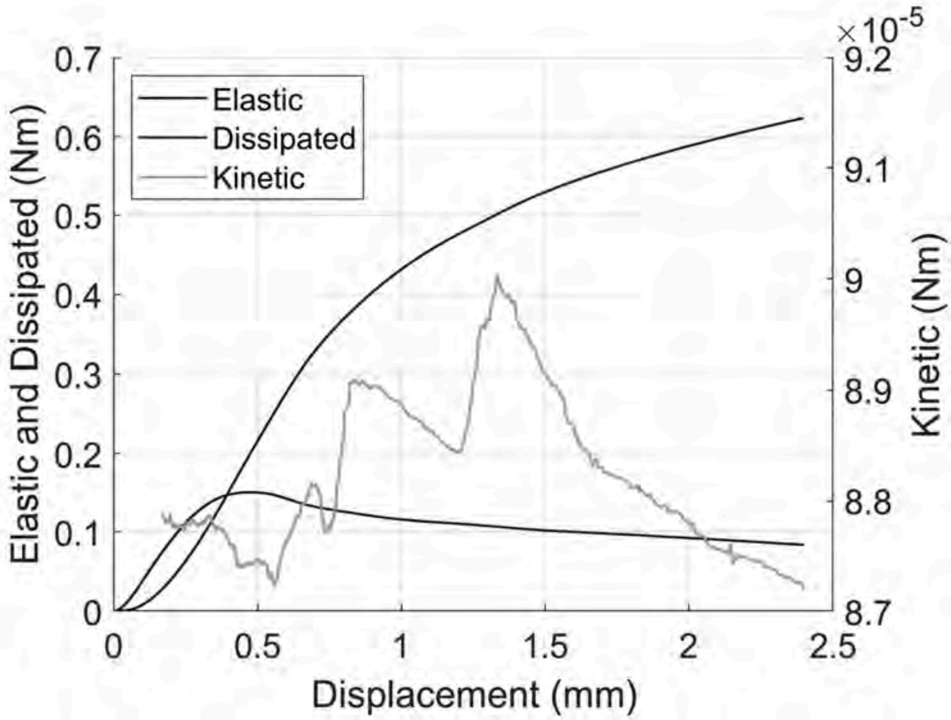

Fig. 15. Energy evolution in the Test 2 simulation.

Table 5
Results of natural frequency simulated by FEM and LDEM - beam with notch.

Set	FEM (Hz)	LDEM (Hz)	Variation (%)
1	458.11	457.38	0.16
2	898.33	903.27	0.55
3	1029.20	1032.10	0.28
4	1267.70	1265.50	0.17
5	1956.70	1957.30	0.03
6	2120.80	2120.30	0.02
7	2191.50	2191.70	0.01
8	2240.50	2234.20	0.28
9	2922.60	2923.70	0.04
10	3113.20	3109.30	0.13

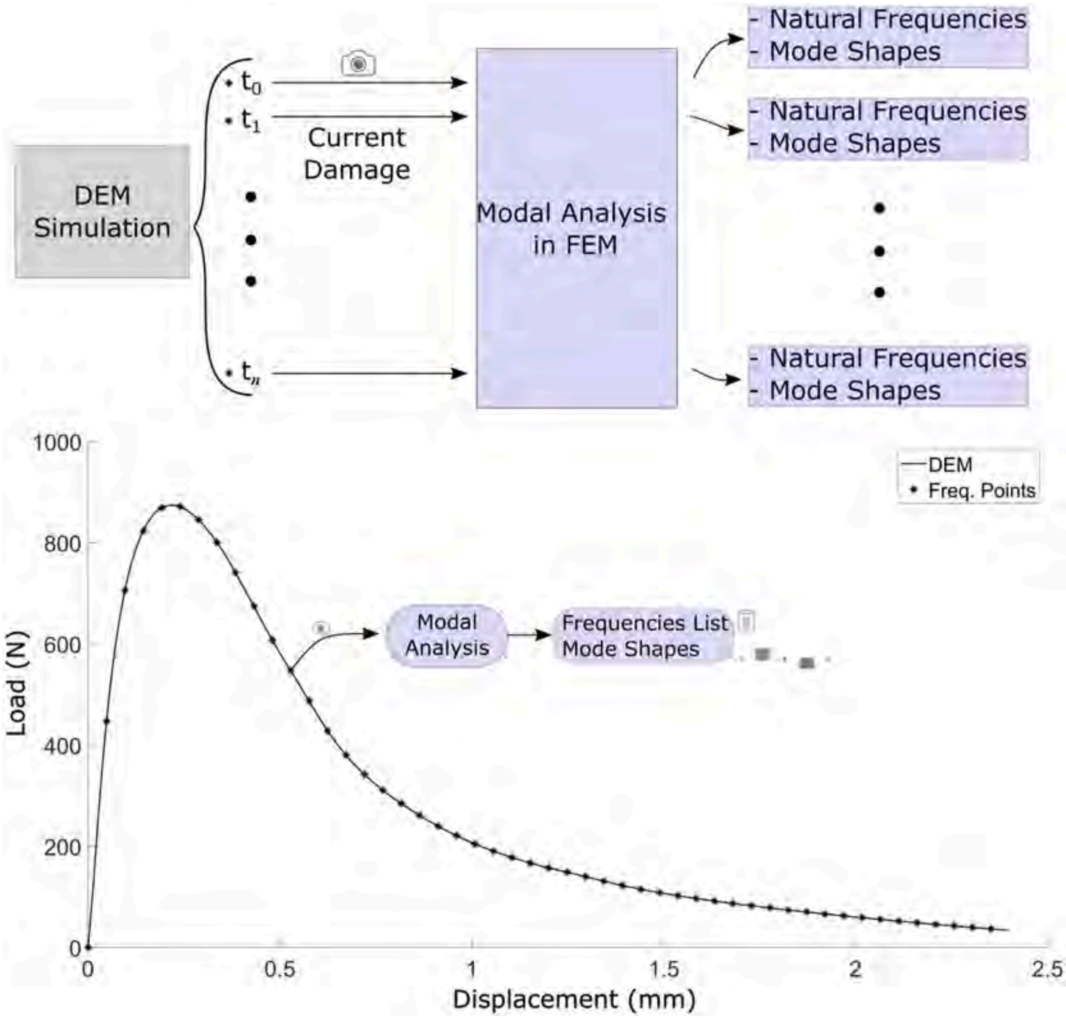

Fig. 16. Methodology for simulating the resonance frequencies and the recorded instants (marked with black asterisks).

should be noted that in the experimental test, this change occurred after the peak load. The reasons for this difference in timing will be investigated in future work.

The resonant frequencies obtained from the simulated test are correlated with the dissipated energy, which quantifies the damage-related energy in the process, in Fig. 19. In this figure, the frequencies are normalized by their initial values, and the dissipated energy is normalized by its maximum value. Fig. 19 also presents the frequency data plotted as a function of the normalized dissipated energy on the horizontal axis. The minimum of the F2/F1 curve occurs at a normalized energy value of 0.064, whereas the maximum load is reached at 0.085. This result indicates that, in the simulation, the onset of modal inversion occurs prior to the peak load, at less than 10% of the beam's total fracture energy capacity.

Fig. 20 presents the numerical mode shapes corresponding to Modes 2, 3, and 10.

Fig. 21 presents the variation of the normalized frequencies obtained in Test 2 for Modes 2, 3, the torsional mode (Mode 6), and Mode 10 (as illustrated in Figs. 6 and 20). The frequency variations are correlated with both the mid-span displacement d and a damage indicator, namely the evolution of the a/h ratio.

The evolution of the a/h ratio was computed using the LDEM model, and the corresponding results are presented in Fig. 19. The equivalent main fissure length, a, was calculated using the expression $a = h - U_d/G_f$. In this expression, h denotes the beam height, U_d represents the dissipated energy obtained from the LDEM energy balance (Fig. 15) and is also used as the horizontal axis in Fig. 19, and G_f is the fracture toughness, an input parameter of the LDEM model listed in Table 4.

It is important to emphasize that, as illustrated in Fig. 14, the damage is not solely concentrated at a single crack tip. Therefore, the value of a should be interpreted as an equivalent crack length.

In this analysis, it is assumed that the variation of the dissipated energy U_d obtained from the simulation is equivalent to the corresponding experimental value. This assumption is supported by the close agreement in both the magnitude and the shape of the load-displacement curves obtained from the experimental and numerical results.

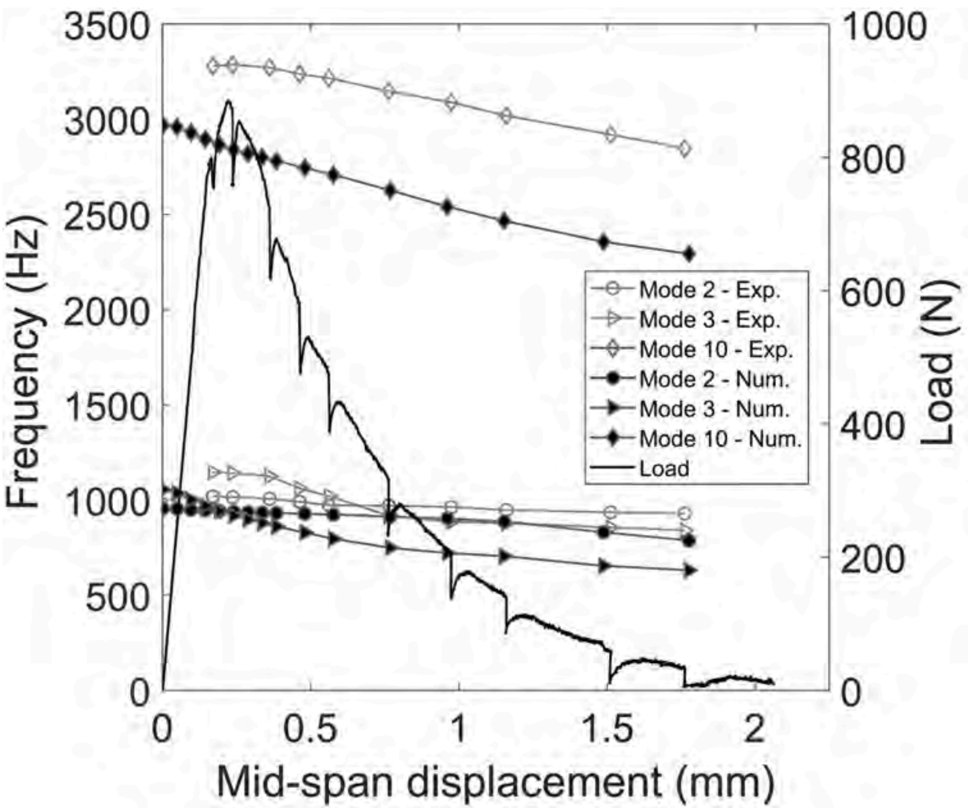

Fig. 17. Experimental and numerical vertical resonant frequency versus displacement curves for Test 2.

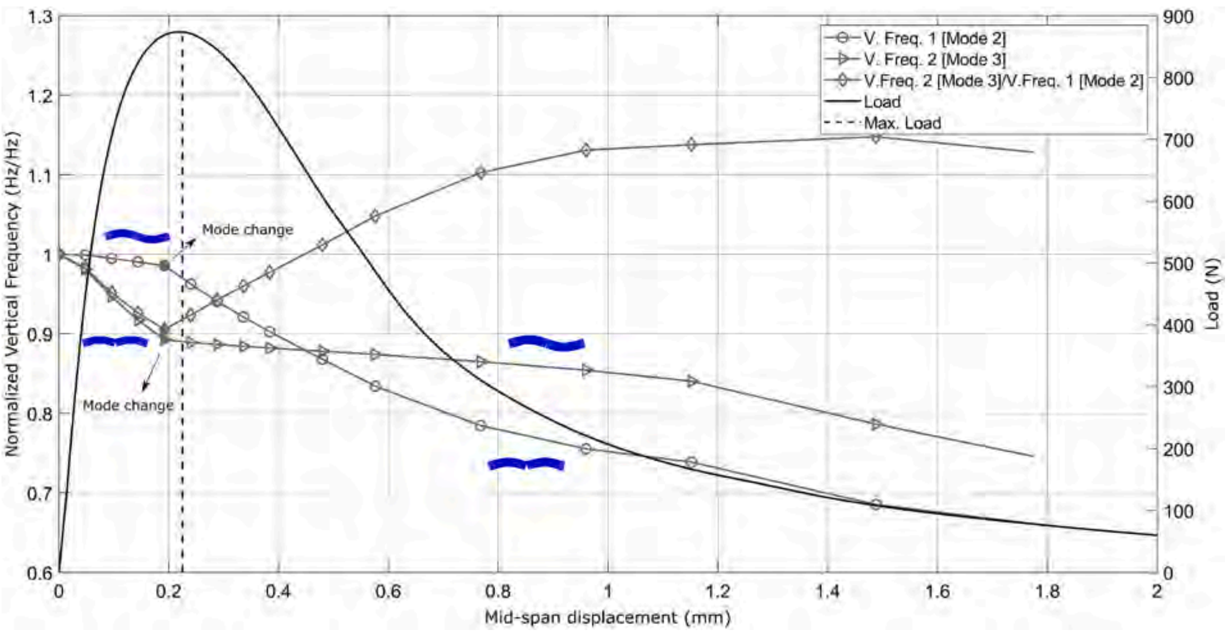

Fig. 18. Evolution of the first two resonance frequencies and numerical load-displacement.

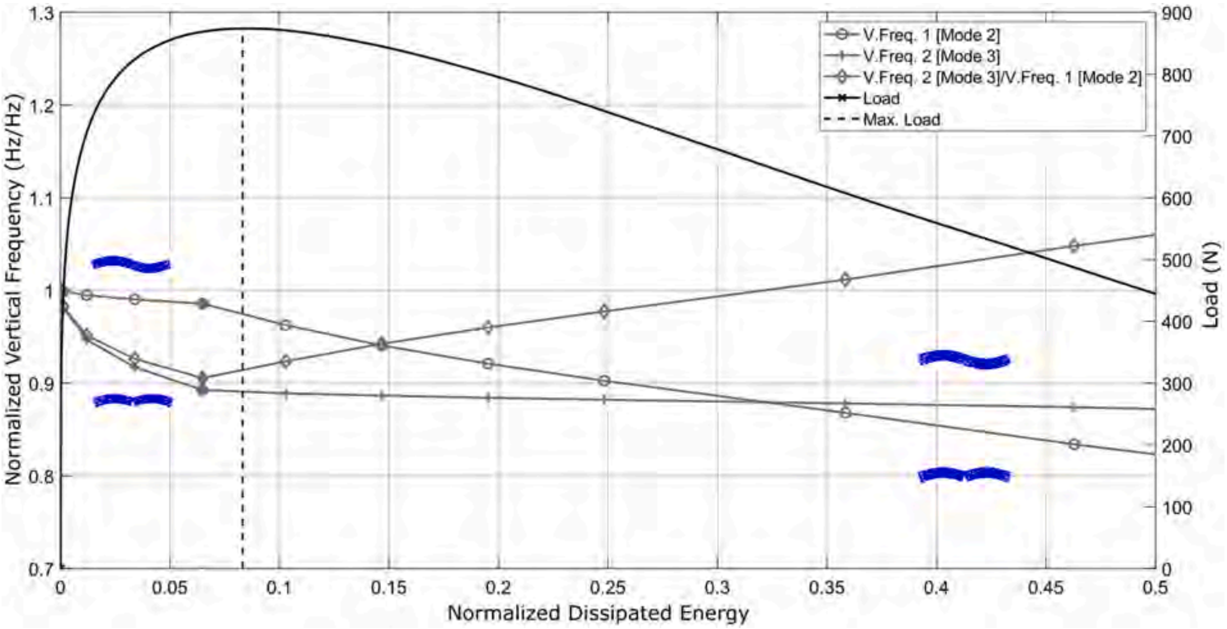

Fig. 19. Evolution of the first two resonant frequencies and the load as a function of the normalized energy.

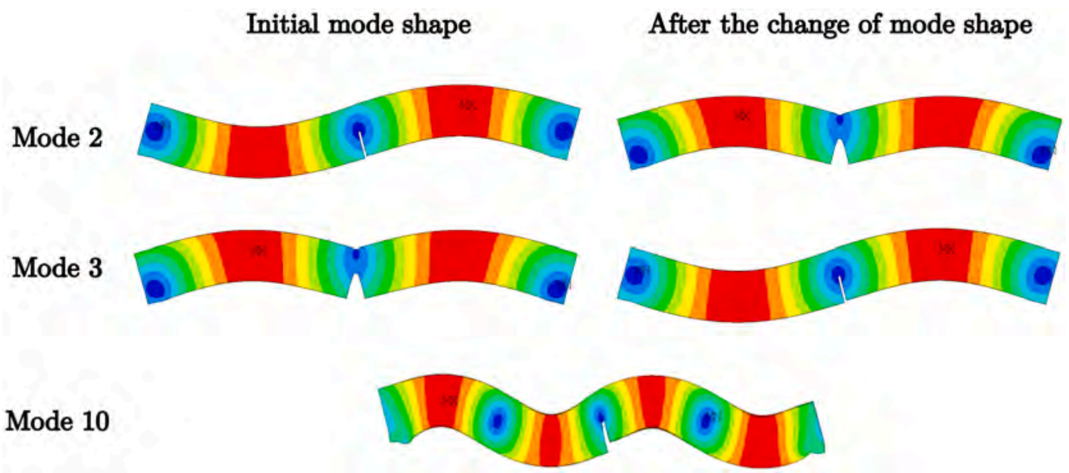

Fig. 20. Vertical vibration modes studied, with an indication of the change in mode shape when it occurs.

Several observations regarding these curves are presented below:

- The natural frequency of the torsional mode (Mode 6, illustrated in Fig. 6) exhibits the most pronounced decrease as damage progresses.
- In Fig. 21a, a mode shift occurs at a displacement of $d = 0.42$ mm, corresponding to a normalized dissipated energy of $a/h = 0.64$, as indicated by the continuous lines in Fig. 21a and b. At this point, Mode 2 transitions from an asymmetric to a symmetric shape. Following this shift, the natural frequency of Mode 2 begins to decrease at an accelerated rate within the interval $a/h \in [0.7, 0.77]$, before returning to its initial rate of decrease. This characteristic point is indicated by the dashed lines in Fig. 21a and b.
- In contrast, the asymmetric Mode 3 exhibits a consistent rate of decrease throughout the entire damage process.
- After the mode switch at $a/h = 0.64$, the rates of frequency decrease for Mode 2 and the torsional mode (Mode 6) are nearly identical.

Figs. 22 and 23 present a comparison between the experimental results and the numerical results obtained from the LDEM simulation. The data points represent measurements recorded at each stop during Test 2. Key observations derived from these results are outlined below.

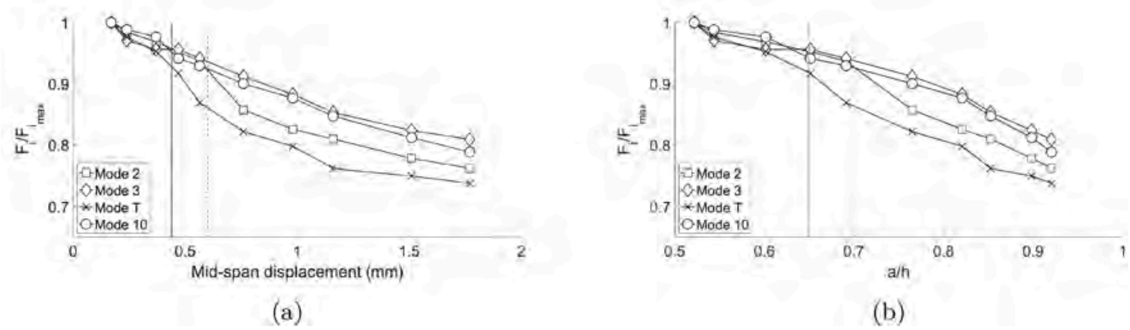

Fig. 21. Normalized natural frequency variations measured in Test 2: (a) as a function of the global displacement and (b) as a function of the equivalent a/h ratio. The continuous line indicates the occurrence of the Mode 2-Mode 3 switch, whereas the dashed line indicates the point at which Mode 2 exhibits a pronounced decrease in frequency.

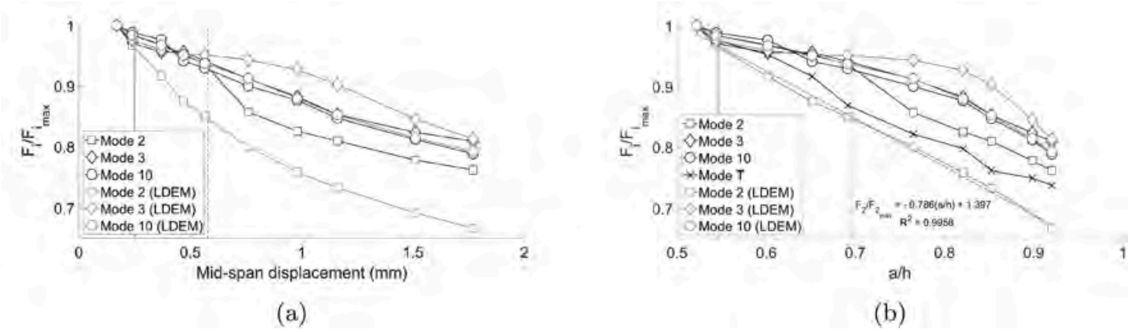

Fig. 22. Comparison between the LDEM simulation and the experimental results from Test 2 for the normalized natural frequencies as a function of (a) the global mid-span displacement and (b) the equivalent a/h ratio.

- A comparison between the experimental and numerical results reveals a notable difference in the evolution of the natural frequencies of Modes 2 and 3 during the damage process. In Fig. 22, vertical dashed lines in orange (experimental) and blue (numerical) indicate the point at which a mode switch from asymmetric to symmetric occurs between Modes 2 and 3.
- The mode switch occurs at different stages: at ($a/h = 0.7$, $d = 0.66$ mm) in the experiment and at ($a/h = 0.55$, $d = 0.17$ mm) in the simulation. One possible explanation for this discrepancy is that the LDEM model lacks the capability to capture the crack-closure effect at the tip of the main fissure as damage progresses. This crack-closure effect is a well-known phenomenon associated with the subcritical growth of cracks, as discussed in classical fracture mechanics texts such as Anderson [50]. This hypothesis will be investigated in future work.
- Despite the differences discussed above, the natural frequency of Mode 2 exhibits a consistent linear decay rate after the mode switch in both the numerical and experimental results. The slope of this decay was computed as −0.79, showing excellent agreement between the experimental and numerical results, as illustrated in Fig. 22b. Furthermore, both datasets exhibit the same decay rate after $a/h = 0.75$.
- When the frequency decrease of Mode 2 is plotted against the global displacement (Fig. 22a), the linear trend is maintained only up to $d = 0.5$ mm, beyond which it is lost. This loss of linearity correlates with the behavior of the damage energy in the simulation's energy balance (Fig. 15), which also becomes non-linear after $d = 0.5$ mm. In contrast, the linear trend is preserved over almost the entire range when the frequency is plotted against the indirect damage measure (the a/h ratio).
- Fig. 23b illustrates the characteristic behavior of the frequency variation of Mode 3. The frequency decreases sharply at first; subsequently, the rate of decay significantly diminishes within the interval $a/h \in [0.6, 0.8]$, and finally increases again after $a/h = 0.8$, forming a typical sigmoidal curve. The experimental results also follow this trend, although it is less pronounced.
- As shown in Figs. 22 and 23c, the experimental and numerical results for the frequency decrease of Mode 10 are in good agreement. This agreement is likely due to the reduced influence of the "closure effect" at the fissure head on this particular mode. It can also be observed that the frequency decrease remains approximately linear up to $a/h = 0.8$, after which the rate of decay becomes more pronounced.

We consider it important to observe here that the frequency crossover, and more generally the way frequencies change during the damage process, depends heavily on the geometry and boundary conditions. Nevertheless, the methodology of investigating the evolution of damage by following the natural frequencies in each case could provide an alternative means of monitoring how damage progression affects the structure being studied.

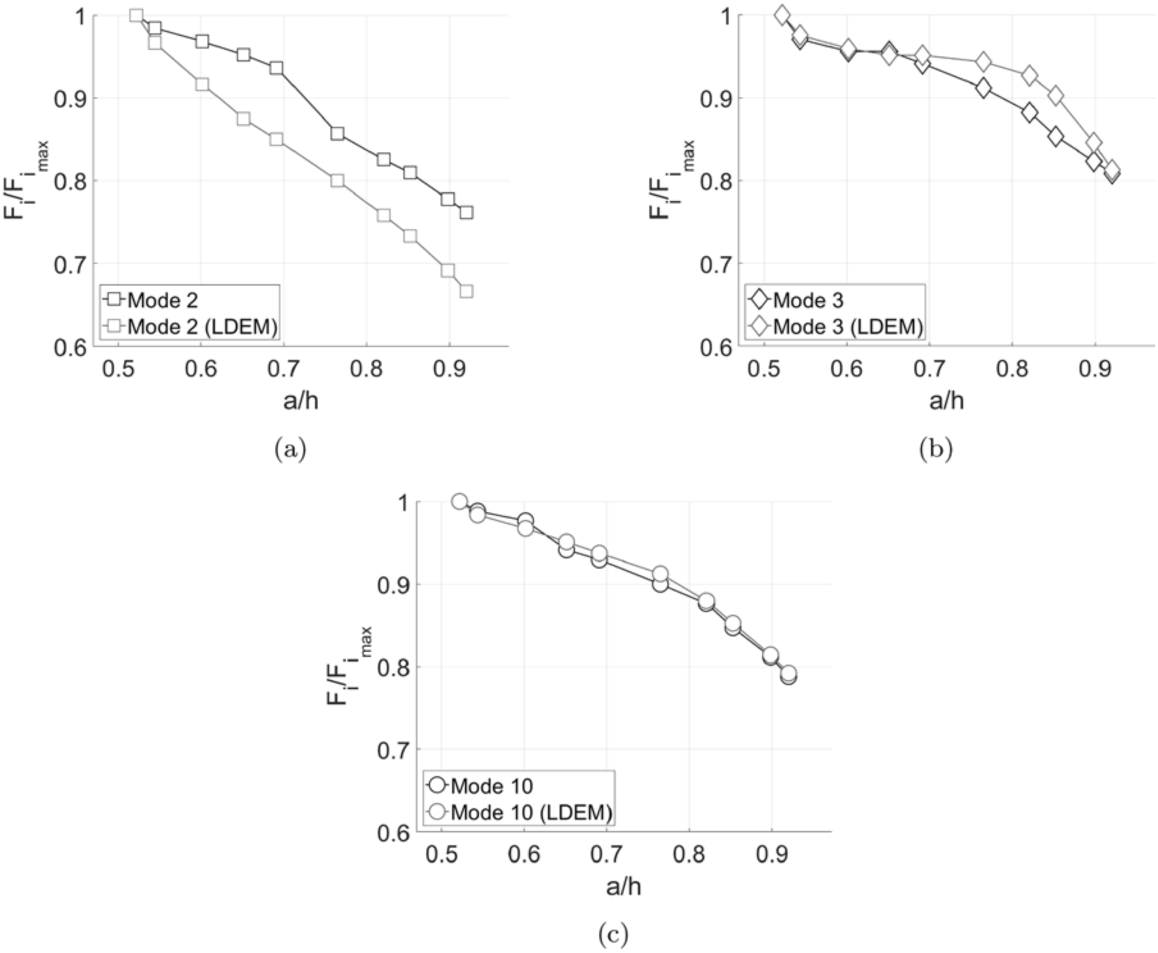

Fig. 23. Comparison between experimental (black) and numerical (gray) results showing the variation of the normalized natural frequencies with increasing damage in the beam. The a/h ratio is used as an indirect but intuitive measure of damage progression in Test 2. (a) Mode 2, (b) Mode 3, (c) Mode 10.

6. Conclusions

This work investigates the variation of vibration frequencies in a prismatic concrete beam subjected to progressive structural damage, with the aim of evaluating whether these frequency changes can serve as predictors of imminent structural failure. The study builds upon the experimental work of [39], who conducted three-point bending tests on notched concrete beams under displacement-controlled loading. In one of these tests, resonant frequencies were recorded at different loading stages using hammer impact excitation and PZT sensors. The present paper complements that prior research by:

(i) Performing a comprehensive analysis of the experimental data acquired during the staged test;
(ii) Demonstrating the potential for accurate mode identification through advanced signal processing techniques;
(iii) Employing the Lattice Discrete Element Method (LDEM) to simulate the nonlinear behavior of the pre-cracked beam and to obtain natural frequencies at intermediate damage states. These states were subsequently analyzed using the Finite Element Method (FEM) to solve an eigenvalue problem and compute the corresponding natural frequencies;
(iv) Presenting a discussion that links damage evolution to frequency reduction, exploring the sensitivity of natural frequencies as potential precursors of damage.

The following conclusions are drawn from this work:

- The methodology outlined in Section 3.3 proved effective in systematically analyzing the comprehensive experimental dataset. By utilizing not only the power spectrum amplitude but also the phase function of the Fourier transform, it was possible to track the variation of natural frequencies and verify that the identified frequencies corresponded to coherent modal shapes.
- The Lattice Discrete Element Method (LDEM) proved to be a valuable tool for interpreting variations in natural frequencies. Although differences between the experimental and numerical results were observed and warrant further investigation, this study

demonstrates how LDEM simulations can enhance the understanding of complex phenomena, particularly when precise replication is not the primary objective.
- The variation of natural frequencies with increasing damage suggests that higher-order modes are less influenced by the "closure effect" at the crack tip. This conclusion will constitute a key focus of subsequent research.
- The characteristic decrease in the frequency of Mode 2 indicates that, after the transition from an asymmetric to a symmetric mode, the decay becomes clearly linear. A slope of $c = -0.79$ was measured, showing excellent agreement between the experimental and numerical results.
- The natural frequency associated with the torsional mode demonstrated strong potential as a damage indicator. Its decrease was both linear and highly sensitive to increasing damage levels, making it a promising candidate for further investigation in the next phase of this research.

CRediT authorship contribution statement

G. Birck: Conceptualization, Methodology, Validation, Formal analysis, Investigation, Data curation, Writing – original draft, Visualization; **G. Piana:** Investigation, Data curation, Writing – review & editing; **W. Almeida:** Software, Validation, Data curation, Writing – original draft, Visualization; **I. Iturrioz:** Validation, Data curation, Writing – original draft, Supervision; **G. Lacidogna:** Conceptualization, Methodology, Investigation, Writing – review & editing, Supervision, Project administration, Funding acquisition.

Declaration of competing interest

The authors declare that they have no known competing financial interests or personal relationships that could have appeared to influence the work reported in this paper.

Acknowledgements

The authors gratefully acknowledge the financial support received from the National Council for Scientific and Technological Development (CNPq - Brazil - Funding Number 309974/2021-6) and the Coordination for the Im-provement of Higher Education Personnel (CAPES - Brazil - Finance Code 001). The authors also wish to thank Politecnico di Torino, Italy, for its sponsorship through basic research funds.

Data availability

Data will be made available on request.

Supplementary material

Supplementary material associated with this article can be found in the online version at 10.1016/j.jsv.2026.120097

References

[1] C.U. Grosse, M. Ohtsu (Eds.), Acoustic Emission Testing, Springer-Verlag, Berlin Heidelberg, 2008.
[2] I. Alqurashi, N. Alver, U. Bagci, F.N. Catbas, A review of ultrasonic testing and evaluation methods with applications in civil NDT/E, J. Nondestruct. Eval. 44 (2025) 53. https://doi.org/10.1007/s10921-025-01190-0
[3] J.L. Rose, Ultrasonic Guided Waves in Solid Media, Cambridge University Press, Cambridge, 2014.
[4] D.J. Ewins, Modal Testing: Theory, Practice and Application, Research Studies Press, Baldock, second ed., 2000.
[5] O.S. Salawu, Detection of structural damage through changes in frequency: a review, Eng. Struct. 19 (9) (1997) 718–723. https://doi.org/10.1016/S0141-0296(96)00149-6
[6] A.K. Pandey, M. Biswas, M.M. Samman, Damage detection from changes in curvature mode shapes, J. Sound Vib. 169 (1) (1994) 3–17. https://doi.org/10.1016/0022-460X(91)90595-B
[7] Q.T. Nguyen, R. Livaoğlu, Damage detection of high-rise buildings using an eigenvalue problem-based inverse solution, Soil Dyn. Earthq. Eng. 152 (2022) 107019. https://doi.org/10.1016/j.soildyn.2021.107019
[8] R. Zhao, R. Yan, Z. Chen, K. Mao, P. Wang, R.X. Gao, Deep learning and its applications to machine health monitoring, Mech. Syst. Signal Process. 115 (2019) 213–237. https://doi.org/10.1016/j.ymssp.2018.05.050
[9] M. Dilena, A. Morassi, Dynamic testing of a damaged bridge, Mech. Syst. Signal Process. 25 (5) (2011) 1485–1507. https://doi.org/10.1016/j.ymssp.2010.12.017
[10] Y. Wang, D.P. Thambiratnam, T.H.T. Chan, A. Nguyen, Method development of damage detection in asymmetric buildings, J. Sound Vib. 413 (2018) 41–56. https://doi.org/10.1016/j.jsv.2017.10.015
[11] F. Aras, F.N. Catbas, Monitoring the changes in the dynamic properties of an RC building experiencing column loss, J. Civ. Struct. Health Monit. 14 (4) (2024) 1257–1274. https://doi.org/10.1007/s13349-024-00783-z
[12] F. Aras, Effects of partial structural damage in the dynamic characteristics of an existing RC building, Earthq. Eng. Eng. Vib. 24 (3) (2025) 781–793. https://doi.org/10.1007/s11803-025-2336-2
[13] S. Kang, M.-Q. Wang, R. Kumar, J.-J. Zhang, Z.-Y. He, Y. Tong, V. Singh, Robust structural damage identification through VMD and feature-level fusion of multi-source vibration signals, Measurement 271 (2026) 120876. https://doi.org/10.1016/j.measurement.2026.120876
[14] Z. Chen, Z. Wang, C. Pan, Z. Ding, Z. Yang, Enhanced axle weight identification via multi-scale feature embedding assisted multi-task neural network, Eng. Struct. 327 (2025) 119616. https://doi.org/10.1016/j.engstruct.2026.122381
[15] Z. Zhu, W. Hu, H. Zhang, J. Cai, Y. Liu, L. Dai, H. Liu, Hierarchical knowledge transfer-based model for missing structural response reconstruction of offshore jacket platform, Ocean Eng. 343 (2026) 123459. https://doi.org/10.1016/j.oceaneng.2025.123459
[16] Z. Chen, Z. Zhang, X. Chen, T. Zhou, Z. Ding, Sparse damage identification for beam-like structures using multiple-metric fusion and nuclear norm regularization, ASCE-ASME J. Risk Uncertain. Eng. Syst. Part A Civ. Eng. 12 (2) (2026) 04026004. https://doi.org/10.1061/AJRUA6.RUENG-1797

[17] A. Koszewnik, K. Lesniewski, V. Pakrashi, Numerical analysis and experimental verification of damage identification metrics for smart beam with MFC elements to support structural health monitoring, Sensors 21 (20) (2021) 6796. https://doi.org/10.3390/s21206796
[18] Y. Lee, H. Kim, S. Min, H. Yoon, Structural Damage Detection Using Deep Learning and FE Model Updating Techniques, Vol. 13, Nature Publishing Group UK, 2023.
[19] P.A. Cundall, O.D.L. Strack, A discrete numerical model for granular assemblies, Géotechnique 29 (1) (1979) 47–65. https://doi.org/10.1680/geot.1979.29.1.47
[20] C. O'Sullivan, Particulate Discrete Element Modelling: A Geomechanics Perspective, CRC Press, London, 2011. https://doi.org/10.1201/9781482266498
[21] R.O. Dror, R.M. Dirks, J.P. Grossman, H. Xu, D.E. Shaw, Biomolecular simulation: a computational microscope for molecular biology, Annu. Rev. Biophys. 41 (2012) 429–452. https://doi.org/10.1146/annurev-biophys-042910-155245
[22] J.R. Perilla, B.C. Goh, C.K. Cassidy, B. Liu, K. Schulten, Molecular dynamics simulations of large macromolecular complexes, Curr. Opin. Struct. Biol. 31 (2015) 64–74. https://doi.org/10.1016/j.sbi.2015.03.007
[23] A.R. Atilgan, S.R. Durell, R.L. Jernigan, M.C. Demirel, O. Keskin, I. Bahar, Anisotropy of fluctuation dynamics of proteins with an elastic network model, Biophys. J. 80 (1) (2001) 505–515. https://doi.org/10.1016/S0006-3495(01)76033-X
[24] D. Scaramozzino, G. Lacidogna, G. Piana, A. Carpinteri, A finite-element-based coarse-grained model for global protein vibration, Meccanica 54 (13) (2019) 1927–1940. https://doi.org/10.1007/s11012-019-01037-9
[25] S.A. Silling, Reformulation of elasticity theory for discontinuities and long-range forces, J. Mech. Phys. Solids 48 (1) (2000) 175–209. https://doi.org/10.1016/S0022-5096(99)00029-0
[26] S.A. Silling, E. Askari, A meshfree method based on the peridynamic model of solid mechanics, Comput. Struct. 83 (17–18) (2005) 1526–1535. https://doi.org/10.1016/j.compstruc.2004.11.026
[27] E. Madenci, E. Oterkus, Peridynamic Theory and Its Applications, Springer, New York, 2014. https://doi.org/10.1007/978-1-4614-8465-3
[28] F. Bobaru, J.T. Foster, P.H. Geubelle, S.A. Silling, (Eds.), Handbook of Peridynamic Modeling, CRC Press, Boca Raton, 2017. https://doi.org/10.1201/9781315373331
[29] W.R. Almeida, B.N.R. Tanzi, G. Birck, I. Iturrioz, G. Lacidogna, Analysis of damage process in a pre-notched rock specimen: the synergy between experimental results and simulations using a peridynamic model, Appl. Sci. 14 (11) (2024) 4721. https://doi.org/10.3390/app14114721
[30] A.P. Jivkov, J.R. Yates, Elastic behaviour of a regular lattice for meso-scale modelling of solids, Int. J. Solids Struct. 49 (22) (2012) 3089–3099. https://doi.org/10.1016/j.ijsolstr.2012.06.010
[31] S. Mastilovic, A. Rinaldi, Two-dimensional discrete damage models: discrete element methods, particle models, and fractal theories, in: G.Z. Voyiadjis (Ed.), Handbook of Damage Mechanics: Nano-to-Macro Scale Concepts for Fracture and Fatigue, Springer, New York, 2015, pp. 273–303. https://doi.org/10.1007/978-1-4614-5589-9_23
[32] A. Jenabidehkordi, Computational methods for fracture in rock: a review and recent advances, Front. Struct. Civ. Eng. 13 (2) (2019) 273–287. https://doi.org/10.1007/s11709-018-0459-5
[33] J.D. Riera, Local effects in impact problems on concrete structures, in: Proceedings of the Conference on Structural Analysis and Design of Nuclear Power Plants, Vol. 3, Porto Alegre, Brazil, 1984, pp. 57–79.
[34] I. Iturrioz, G. Lacidogna, A. Carpinteri, Acoustic emission detection in concrete specimens: experimental analysis and lattice model simulations, Int. J. Damage Mech. 23 (3) (2014) 327–358. https://doi.org/10.1177/1056789513494232
[35] G. Birck, J.D. Riera, I. Iturrioz, Numerical DEM simulation of AE in plate fracture and analogy with the frequency of seismic events in SCRs, Eng. Fail. Anal. 93 (2018) 214–223. https://doi.org/10.1016/j.engfailanal.2018.06.024
[36] B.N.R. Tanzi, M. Sobczyk, I. Iturrioz, G. Lacidogna, Damage evolution in quasi-brittle materials: experimental analysis by AE and numerical simulation, Appl. Sci. 13 (19) (2023) 10947. https://doi.org/10.3390/app131910947
[37] I. Iturrioz, J.D. Riera, Assessment of the lattice discrete element method in the simulation of wave propagation in inhomogeneous linearly elastic geologic materials, Soil Dyn. Earthquake Eng. 151 (2021) 106952. https://doi.org/https://doi.org/10.1016/j.soildyn.2021.106952
[38] G. Lacidogna, G. Piana, A. Carpinteri, Acoustic emission and modal frequency variation in concrete specimens under four-point bending, Appl. Sci. 7 (4) (2017) 339. https://doi.org/10.3390/app7040339
[39] G. Lacidogna, G. Piana, A. Carpinteri, Damage monitoring of three-point bending concrete specimens by acoustic emission and resonant frequency analysis, Eng. Fract. Mech. 210 (2019) 402–413. https://doi.org/10.1016/j.engfracmech.2018.06.034
[40] A.H. Nayfeh, M.S. Hefzy, Continuum modeling of three-dimensional truss-like space structures, AIAA J. 16 (8) (1978) 779–787. https://doi.org/10.2514/3.7581
[41] L.E. Kosteski, I. Iturrioz, D.R. Barrios, Crack propagation in elastic solids using the truss-like discrete element method, Int. J. Fract. 174 (2) (2012) 139–161. https://doi.org/10.1007/s10704-012-9684-4
[42] A. Hillerborg, A Model for Fracture Analysis, Technical Report TVBM-3005, Division of Building Materials, Lund Institute of Technology, Lund University, Lund, Sweden, 1978.
[43] V.B. Puglia, L.E. Kosteski, J.D. Riera, I. Iturrioz, Random field generation of the material properties in the lattice discrete element method, J. Strain Anal. Eng. Des. 54 (4) (2019) 211–228. https://doi.org/10.1177/0309324719858849
[44] J.D. Riera, I. Iturrioz, Discrete element model for evaluating impact and impulsive response of reinforced concrete plates and shells subjected to impulsive loading, Nucl. Eng. Des. 179 (2) (1998) 135–144. https://doi.org/10.1016/S0029-5493(97)00270-7
[45] L.E. Kosteski, J.D. Riera, I. Iturrioz, R.K. Singh, T. Kant, Analysis of reinforced concrete plates subjected to impact employing the truss-like discrete element method, Fatigue Fract. Eng. Mater. Struct. 38 (3) (2015) 276–289. https://doi.org/10.1111/ffe.12227
[46] L.A. Dalguer, K. Irikura, J.D. Riera, Simulation of tensile crack generation by three-dimensional dynamic shear rupture propagation during an earthquake, J. Geophys. Res. Solid Earth 108 (B3) (2003) 2144. https://doi.org/10.1029/2001JB001738
[47] RILEM Draft recommendation, TC 50-FMC, determination of the fracture energy of mortar and concrete by means of three-point bend tests on notched beams, Mater. Struct. 18 (4) (1985) 285–290. https://doi.org/10.1007/BF02472917
[48] Ministero delle Infrastrutture e dei Trasporti, D. M. 14/01/2008 - Norme Tecniche per le Costruzioni, 2008, (Gazzetta Ufficiale della Repubblica Italiana 29 (30)) (in Italian).
[49] ANSYS Inc., ANSYS Theory Reference Manual, 2021. https://doi.org/10.1201/9781420058215
[50] T.L. Anderson, Fracture Mechanics: Fundamentals and Applications, CRC Press, Boca Raton, FL, 3rd ed., 2005. https://doi.org/10.1201/9781420058215